



Paper

Cite this article: Sergienko OV, Wingham DJ (2019). Grounding line stability in a regime of low driving and basal stresses. *Journal of Glaciology* **65**, 833–849. <https://doi.org/10.1017/jog.2019.53>

Received: 4 January 2019

Revised: 20 July 2019

Accepted: 22 July 2019

First published online: 12 September 2019

Keywords:

Ice dynamics; ice-sheet modeling; ice streams

Author for correspondence:

O. V. Sergienko, E-mail: osergien@princeton.edu

Grounding line stability in a regime of low driving and basal stresses

O. V. Sergienko¹ and D. J. Wingham²

¹Atmospheric and Oceanic Sciences Program, Princeton University, 300 Forrester Rd., Princeton, NJ, 08542 and

²The Natural Environment Research Council, Polaris House, North Star Avenue, Swindon, SN2 1EU, UK

Abstract

The dynamics of a marine ice sheet's grounding lines determine the rate of ice discharge from the grounded part of ice sheet into surrounding oceans. In many locations in West Antarctica ice flows into ice shelves through ice streams experiencing low driving stress. However, existing simple theories of marine ice sheets are developed under the assumption of high basal and driving stress. Here we analyze the grounding line behavior of marine ice streams experiencing low basal shear and driving stress. We find that in this regime, the ice flux at the grounding line is a complex function of the geometry of the ice-stream bed, net accumulation rate and gradient of the net accumulation rate. Our analysis shows that the stability of distinct steady states is determined by the same parameters, suggesting a more complex (in)stability criterion than what is commonly referred to within the context of the 'marine ice-sheet instability hypothesis'. We also determine characteristic timescales (*e*-folding time) of ice-sheet configurations perturbed from their steady states. These timescales can be used to determine whether particular configurations can be considered in isolation from other components of the climate system or whether their effects and feedbacks between the ice sheet and the rest of the climate system have to be taken into account.

Introduction

Determining the location and the rate of migration of the grounding line – a transition between the grounded part of a marine ice sheet and its floating ice shelf – is a fundamental question in understanding ice-sheet interactions with the rest of the climate system. In circumstances in which the characteristic scales of ice-sheet internal processes are short in comparison with those of wider climate variability, it is possible to consider ice sheets as an isolated system and, through investigation of the stability of their steady-state configurations, learn about their intrinsic processes, specific to ice dynamics, and unrelated to the external climate variability. Weertman (1974) was the first to provide a theoretical description of stability of steady-state marine ice sheets. He concluded that 'A stable ice sheet can occur if the bed slopes away from the center of the ice sheet. The generalization of our results to other bed shapes is rather obvious.' The potential practical importance of this statement has resulted in a number of more detailed investigations (e.g., Chugunov and Wilchinsky, 1996; Schoof, 2007b; Nowicki and Wingham, 2008; Tsai and others, 2015; Favier and others, 2016; Haseloff and Sergienko, 2018). In particular, using matched asymptotic expansions, Schoof (2007b) has developed a boundary layer theory for an ice stream undergoing rapid sliding at its grounding line. In circumstances where the grounded ice sheet and floating ice shelf are laterally unconfined, the steady-state ice flux at the grounding line is a single-valued monotonically increasing function of ice thickness at the grounding line (Schoof, 2007b; Tsai and others, 2015). Using the results of this theory Schoof (2012) performed a linear stability analysis, whose result confirmed Weertman's heuristic argument that the grounding lines on retrograde beds (the bed elevation increases in the direction of ice flow) are unstable. This outcome is widely known as the 'marine ice-sheet instability hypothesis'.

While these studies have considered two distinct types of flow of the grounded ice, one dominated by vertical shear (e.g., Weertman, 1974; Nowicki and Wingham, 2008; Wilchinsky, 2009), and the other one dominated by basal sliding (e.g., Schoof, 2007b; Tsai and others, 2015), their common assumptions are that the driving stress is of the same order as the basal stress, and that both are larger than the divergence of the longitudinal stress. At the grounding line the longitudinal stress must balance the hydrostatic pressure. Satisfying these two balances led Schoof (2007b) to the conclusion that the ice thickness at the grounding line must be small in comparison with the ice thickness in the interior, with the consequence that the ice thickness gradient is large in the vicinity of the grounding line. However, this is in marked contrast to the observed low surface gradients (Rose, 1979; MacAyeal and others, 1995) of many present-day West Antarctic ice streams, particularly those which flow to the Ross Ice Shelf (Fig. 1). Tsai and others (2015) have proposed that the absence of the large surface gradient is a consequence of the Coulomb friction regime in the well-lubricated environment near the grounding line, but these gradients, which are of the order of $1\text{--}5\cdot 10^{-3}$ (Fig. 1a), extend over hundreds of kilometers and do not exhibit significant changes in the vicinity of the grounding line (Fig. 1c). This suggests that these ice streams are characterized by extremely weak beds over extended distances (MacAyeal, 1989), and this leads us to the view that

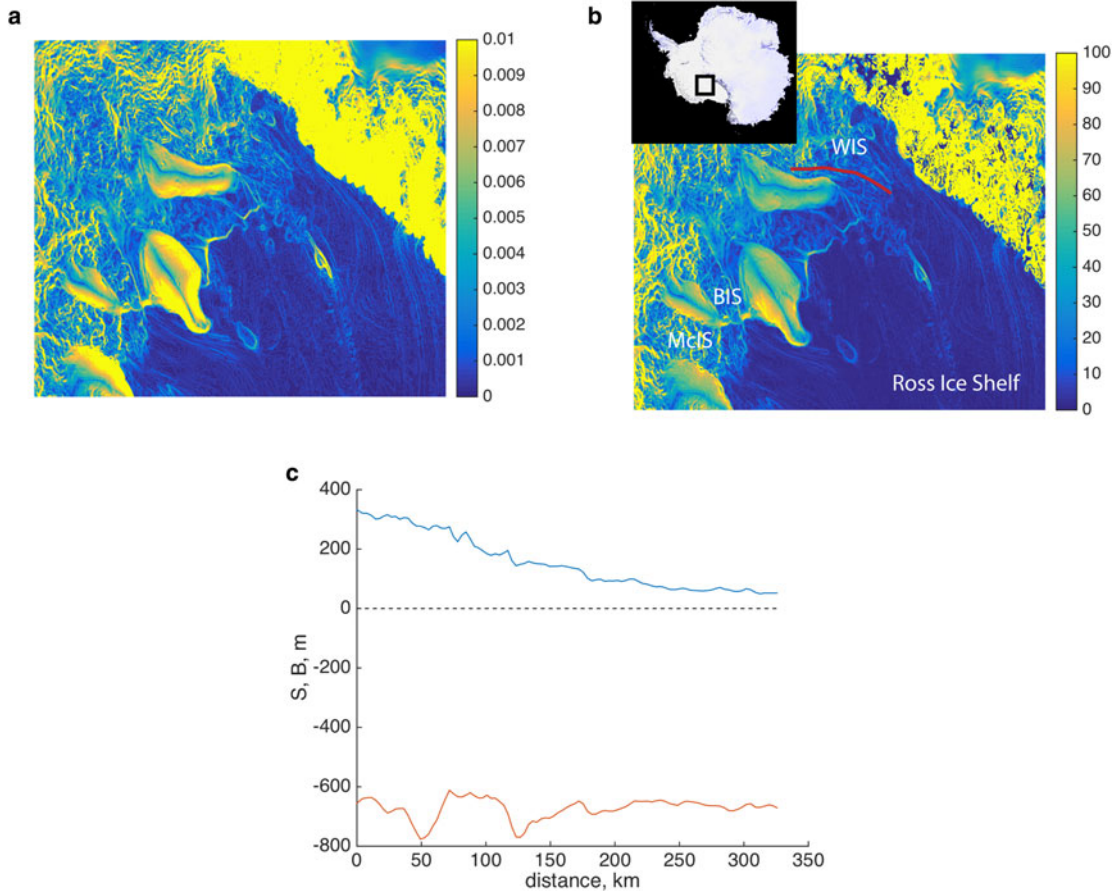


Fig. 1. Characteristics of Siple Coast ice streams. (a) Magnitude of the surface gradient $|\nabla S|$; (b) magnitude of the driving stress (kPa) computed as $\tau_d = \rho g H |\nabla S|$ derived from BEDMAP 2 data set (Fretwell and others, 2013); (c) surface (blue line) and bed (red line) elevation along a flowline on Willans Ice Plain (red line in panel (b)). Siple Coast ice streams: MclS – MacAyeal Ice Stream; BIS – Bindschadler Ice Stream; WIS – Whillans Ice Stream. Their driving stress is in ~ 0 –20 kPa limit. Inset shows the map of Antarctica (Haran and others, 2005), black rectangle shows the location of the Siple Coast region.

analyzing the stability of these ice streams requires a reconsideration of the balance of the terms in the momentum balance.

Using analytical and numerical models, we examine the same configuration of an unconfined ice stream floating into an unconfined ice shelf as considered by Schoof (2007b) and Tsai and others (2015), but extend the analysis to a regime in which the basal shear is on the same order of magnitude as the divergence of extensional stress through the whole length of the ice stream. Our results show that steady-state configurations of marine ice streams are substantially different from those in the regime of strong basal and driving stress. In the regime of low or absent basal shear, ice surface slopes, and consequently the driving stress, are small through the length of the ice stream, and not only in the vicinity of the grounding line. Their flow is controlled by the effects of the bed geometry – elevation, slopes and curvature – that here we collectively term ‘form drag’, basal drag, the accumulation rate, its gradients and higher derivatives. We find that at the grounding line, the ice flux is a multivalued implicit function of ice thickness. Our analysis show that the stability of distinct steady-state configurations is determined by the sign of a parameter denoted Λ that depends on form drag, basal shear, accumulation rate and their first and higher derivatives. In contrast to the marine ice-sheet instability hypothesis that suggests that, in the case of net accumulation, ice sheets are stable on prograde beds only (the bed elevation decreases in the direction of ice flow), ice streams experiencing low basal shear can be both stable ($\Lambda < 0$) and unstable ($\Lambda > 0$) on prograde and retrograde beds. We also find that the reciprocal of the stability parameter Λ can be interpreted in terms of the e -folding time of perturbed steady-state configurations,

and thus $|\Lambda|^{-1}$ indicates how fast or slow this perturbed configuration returns to or evolves from, their steady states. It provides a measure as to whether the evolution of the perturbed configurations can be viewed as insensitive to climate variability.

Model description

We consider an unconfined ice stream that flows into an unconfined ice shelf (Fig. 2) and use the model formulation of Schoof (2007b), which we briefly describe below. Under assumptions of negligible vertical shear appropriate for ice stream and ice shelf flow (MacAyeal, 1989), the vertically integrated momentum balance is

$$2(A^{-(1/n)}h|u_x|^{(1/n)-1}u_x)_x - \tau_b - \rho gh(h+b)_x = 0, \quad (1a)$$

$$x_d \leq x \leq x_j,$$

$$2(A^{-(1/n)}h|u_x|^{(1/n)-1}u_x)_x - \rho g' h h_x = 0, \quad x_j \leq x \leq x_c, \quad (1b)$$

where $u(x)$ is the depth-averaged ice velocity, $h(x)$ ice thickness, $b(x)$ is the bed elevation (negative below sea level and positive above sea level), $A^{-1/n}$ is the ice stiffness parameter (assumed to be constant), n is an exponent of Glen’s flow law, g is the acceleration due to gravity, τ_b is basal shear, g' is the reduced gravity defined as

$$g' = \delta g \quad (2)$$

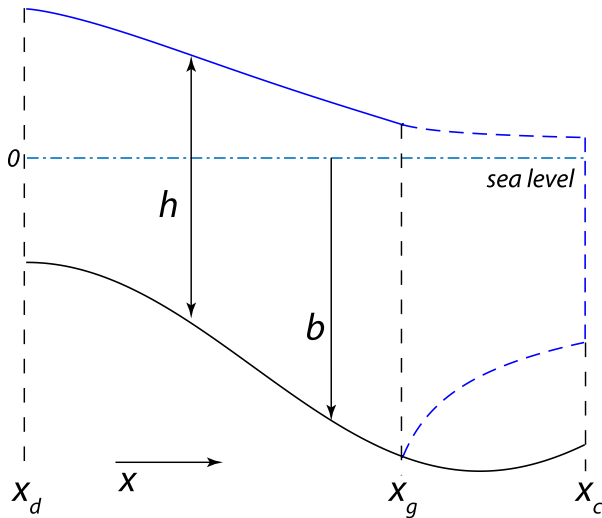


Fig. 2. Model geometry: b – bed elevation ($b < 0$), h – ice thickness, x_d – the ice divide location, x_g – the grounding line location; x_c – the calving front location.

where

$$\delta = \frac{\rho_w - \rho}{\rho_w} \tag{3}$$

is the buoyancy parameter, ρ and ρ_w are the densities of ice and water, respectively, x_d is the location of the ice divide (assumed to be $x_d = 0$), x_c is the location of the calving front and x_j is the location of the junction between the ice stream and ice shelf. In the absence of a universal ‘sliding law’ – a relationship between shear at the ice/bed interface and characteristics of ice and bed – several formulations are commonly used. Throughout the derivations presented below we adopt a formulation used by Schoof (2007b)

$$\tau_b = C|u|^{m-1}u, \tag{4}$$

where C and m are constant parameters. The first term in (1a) is the divergence of the extensional, or longitudinal stress, τ_x , the second term is the basal shear, τ_b , and the final terms in the both equations are the driving stress, τ_d .

The mass balance is

$$h_t + (uh)_x = \begin{cases} \dot{a} & 0 \leq x \leq x_j \\ \dot{m} & x_j < x \leq x_c, \end{cases} \tag{5}$$

where \dot{a} and \dot{m} are the net accumulation/ablation (positive for accumulation) rates of the ice stream and ice shelf, respectively. (The discontinuity at the junction x_j is due to the fact that basal ablation by the ocean is possibly discontinuous across the junction.)

The boundary conditions are

$$(h + b)_x = 0, \quad u = 0, \quad x = 0 \tag{6a}$$

$$2A^{-(1/n)}h|u_x|^{(1/n)-1}u_x = \frac{1}{2}\rho g' h^2, \quad x = x_c. \tag{6b}$$

The condition at the calving front, x_c , requires the longitudinal stress in the ice to balance the pressure deficit at the front. The conditions at the divide, x_d , are statements that there is no driving stress there, and that no flow enters or leaves the domain from the left. These are the natural conditions to describe a divide. A

detailed treatment near the divide in fact requires the solution of a full-Stokes problem (Fowler, 1992). However, the primary concern of this paper is not the detailed behavior near the divide, and we will use (1)–(6), as a sufficient description.

At the junction, x_j continuity conditions have to be prescribed. The number of conditions is determined by the number of the boundary conditions for the ice stream and the ice shelf.

$$u_{\text{stream}}(x_j) = u_{\text{shelf}}(x_j) \tag{7a}$$

$$h_{\text{stream}}(x_j) = h_{\text{shelf}}(x_j) \tag{7b}$$

$$\tau_{\text{stream}}(x_j) = \tau_{\text{shelf}}(x_j). \tag{7c}$$

The problems (1)–(7) provide solutions for any given location of the junction x_j . However, the solution $h(x_j)$ must in addition satisfy the flotation condition

$$h(x_j) = -\frac{\rho_w}{\rho}b(x_j). \tag{8}$$

The grounding line location x_g is then determined as the root of this equation in x_j . We will use the symbols h_g , u_g and τ_g to mean ice thickness, velocity and the longitudinal stress at the grounding line.

Additionally, the following inequalities have to be satisfied

$$h(x) > -\frac{\rho_w}{\rho}b(x), \quad 0 < x < x_g, \tag{9a}$$

$$h(x) \leq -\frac{\rho_w}{\rho}b(x), \quad x_g \leq x < x_c. \tag{9b}$$

These conditions reflect the fact that the ice stream is grounded and the ice shelf is floating. Similar to all previous studies of unconfined ice shelves (e.g., MacAyeal and Barcilon, 1988; Schoof, 2007b) we integrate the momentum balance of the ice shelf (1b), and using the boundary condition at the calving front, x_c , (6b) and the continuity conditions at the grounding line (7), and reduce the problem to the ice stream part only, with the boundary conditions at the grounding line – the flotation condition (8) and the stress condition

$$2A^{-(1/n)}h|u_x|^{(1/n)-1}u_x = \frac{1}{2}\rho g' h^2, \quad x = x_g. \tag{10}$$

The model (1)–(10) is identical to one used by Schoof (2007b).

In what follows we use precise numerical solutions of (1)–(10) to compare with approximate asymptotic expressions, and describe them as ‘exact’, acknowledging their numerical origin. To obtain the ‘exact’ solutions, we use the finite-element solver *Comsol*TM, (COMSOL, 2018), whose accuracy is well-established (e.g. Schäfer and Turek, 1996).

We now proceed to non-dimensionalize (1)–(10) using as characteristic scales the bathymetry of a continental shelf [b], the length of an ice steam [x] and its velocity [u]. In terms of these

$$[h] = [b], \quad [\dot{a}] = \frac{[b][u]}{[x]}, \quad [t] = \frac{[x]}{[u]}. \tag{11}$$

With the two non-dimensional parameters

$$\varepsilon = \frac{2A^{-(1/n)}[u]^{1/n}}{\rho g[h][x]^{1/n}} \tag{12a}$$

$$\gamma = \frac{[C][u]^m[x]}{\rho g[h]^2}, \tag{12b}$$

relating to deformation and sliding, respectively, the non-dimensional momentum balance and mass balance become

$$\begin{aligned} \varepsilon(h|u_x|^{(1/n)-1}u_x)_x - \gamma|u|^{m-1}u - h(h+b)_x &= 0, \\ 0 \leq x \leq x_g, \quad h &\leq -\frac{b}{1-\delta} \end{aligned} \tag{13}$$

and

$$h_t + (uh)_x = \dot{a}, \quad 0 \leq x \leq x_g. \tag{14}$$

The non-dimensional boundary conditions at $x = 0$ and $x = x_g$ are

$$(h+b)_x = 0, \quad u = 0, \quad x = 0 \tag{15a}$$

$$\varepsilon h|u_x|^{(1/n)-1}u_x = \frac{1}{2}\delta h^2, \quad x = x_g, \tag{15b}$$

$$h = -\frac{b(x)}{1-\delta} \quad x = x_g. \tag{15c}$$

The inequality constraint (9) is

$$h(x) > -\frac{b(x)}{1-\delta}, \quad 0 < x < x_g. \tag{16}$$

The non-dimensional problem (13)–(16) has three non-dimensional parameters: ε , expression (12a), γ , expression (12b) and δ , expression (3). Their magnitudes are determined by the characteristic scales of the problem. The buoyancy parameter δ , defined by (3), is determined by the values of densities of ice, $\rho = 917 \text{ kg m}^{-3}$, and sea-water, $\rho_w \approx 1020 \text{ kg m}^{-3}$, which results in $\delta \approx 0.1$. To determine the value of ε , we take as the characteristic scales for the present-day Antarctic ice streams to be $D = 1000 \text{ m}$, $L = 500 \text{ km}$ and $V = 500 \text{ m a}^{-1}$ (Fretwell and others, 2013) together with the ice rheological parameters $n = 3$ and $A = 1.35 \cdot 10^{-25} \text{ Pa}^{-3} \text{ s}^{-1}$ (that corresponds to the ice temperature $T = -20^\circ\text{C}$). These then provide the value for parameter ε is $\sim 1.4 \cdot 10^{-2} \ll 1$.

The choice of γ is not determined by direct observations, because the basal shear, τ_b , is not directly observed, and must be inferred from the surface observations, e.g., by means of inversion techniques from surface observations (e.g. MacAyeal, 1992; Sergienko and others, 2008; Sergienko and Hindmarsh, 2013). We obtain a value of C based on the results of limited direct observations of the basal conditions (e.g., Engelhardt and others, 1990) and results of inverse modeling studies (e.g. MacAyeal, 1992; MacAyeal and others, 1995; Joughin and others, 2004; Sergienko and others, 2014) indicating that basal shear under ice streams has small magnitudes. For instance, using Stokes' equations as a forward model, Sergienko and others (2014) find that the inferred values of the basal shear in the trunks of MacAyeal and Bindshadler ice streams is $\sim 0.5\text{--}5 \text{ kPa}$. Consequently, characteristic scales of the sliding parameter C

are $2 \cdot 10^4\text{--}2 \cdot 10^5 \text{ Pa m}^{-1/3} \text{ s}^{1/3}$, and according to (12b), $\gamma \sim 2.8 \cdot 10^{-2} \text{--} 2.8 \cdot 10^{-1}$.

We seek to provide an approximate solution of the problem (13)–(16), and this requires us to assign relative orders or the three parameters, ε , γ and δ .

As shown above ε and γ are naturally regarded as small, and we take $\varepsilon \sim \gamma \sim o(1)$; but the choice of the order of δ is open to us. One choice is to follow Schoof (2007b) and take δ as $O(1)$. As we noted in section 'Introduction', this leads, as a consequence of the resulting imbalance of terms in the boundary condition (15b), to suppose the existence of a boundary layer close to x_g in which the longitudinal and basal stress terms in the momentum balance (13) are of the same order as the driving stress (Schoof, 2007b; Tsai and others, 2015). The alternative is to take δ as a small parameter, and, indeed, with our choice of scales δ is closer to ε than to unity. We accordingly take $\delta \sim \varepsilon$. This will remove the need for a boundary layer at the junction. The effectiveness of this assignment may be judged from the numerical results we describe later.

The problem can then be reduced to one in which δ is the sole parameter through rescaling in the following fashion using the parameter ε/δ :

$$\begin{aligned} h &= \left(\frac{\varepsilon}{\delta}\right)^\alpha H, \quad b = \left(\frac{\varepsilon}{\delta}\right)^\alpha B, \quad u = \left(\frac{\varepsilon}{\delta}\right)^\beta U, \quad x = \left(\frac{\varepsilon}{\delta}\right)^\kappa X, \\ t &= \left(\frac{\varepsilon}{\delta}\right)^\sigma T. \end{aligned} \tag{17}$$

Substituting these expressions into the momentum balance (13), mass balance (14) and the boundary conditions (15), balancing the first and second terms $(1 + \alpha - \kappa + ((\beta - \kappa)/n) = 1 + m\beta)$ in the momentum balance, all terms in the mass balance $(\alpha - \sigma = \alpha + \beta - \kappa = 0)$, and the both sides in the stress (15b) condition at x_g $(1 + \alpha + ((\beta - \kappa)/n) = 2\alpha)$ we get

$$\begin{aligned} \alpha &= \sigma = \frac{n}{n+1}, \quad \beta = -\frac{1}{(m+1)(n+1)} \left(= -\frac{n}{n+1} \right), \\ \kappa &= \frac{n(m+1) - 1}{(m+1)(n+1)} (= 0), \end{aligned} \tag{18}$$

where expressions in parentheses are for the case of $\gamma = 0$, so that, in this case, x does not need rescaling. The rescaled problem becomes

$$\delta(H|U_X|^{(1/n)-1}U_X)_X - \delta\Gamma|U|^{m-1}U - H(H+B)_X = 0, \tag{19a}$$

$$H_T + (UH)_X = \dot{a} \tag{19b}$$

$$(H+B)_X = 0, \quad U = 0, \quad X = 0 \tag{19c}$$

$$H|U_X|^{(1/n)-1}U_X = \frac{1}{2}H^2, \quad X = X_g \tag{19d}$$

$$H = -\frac{B}{1-\delta} \quad X = X_g \tag{19e}$$

$$H > -\frac{B}{1-\delta}, \quad 0 < X < X_g \tag{19f}$$

where $\Gamma = \gamma/\varepsilon$ and the subscripts X and T are derivatives with respect to the coordinate X and time T . In contrast to the original

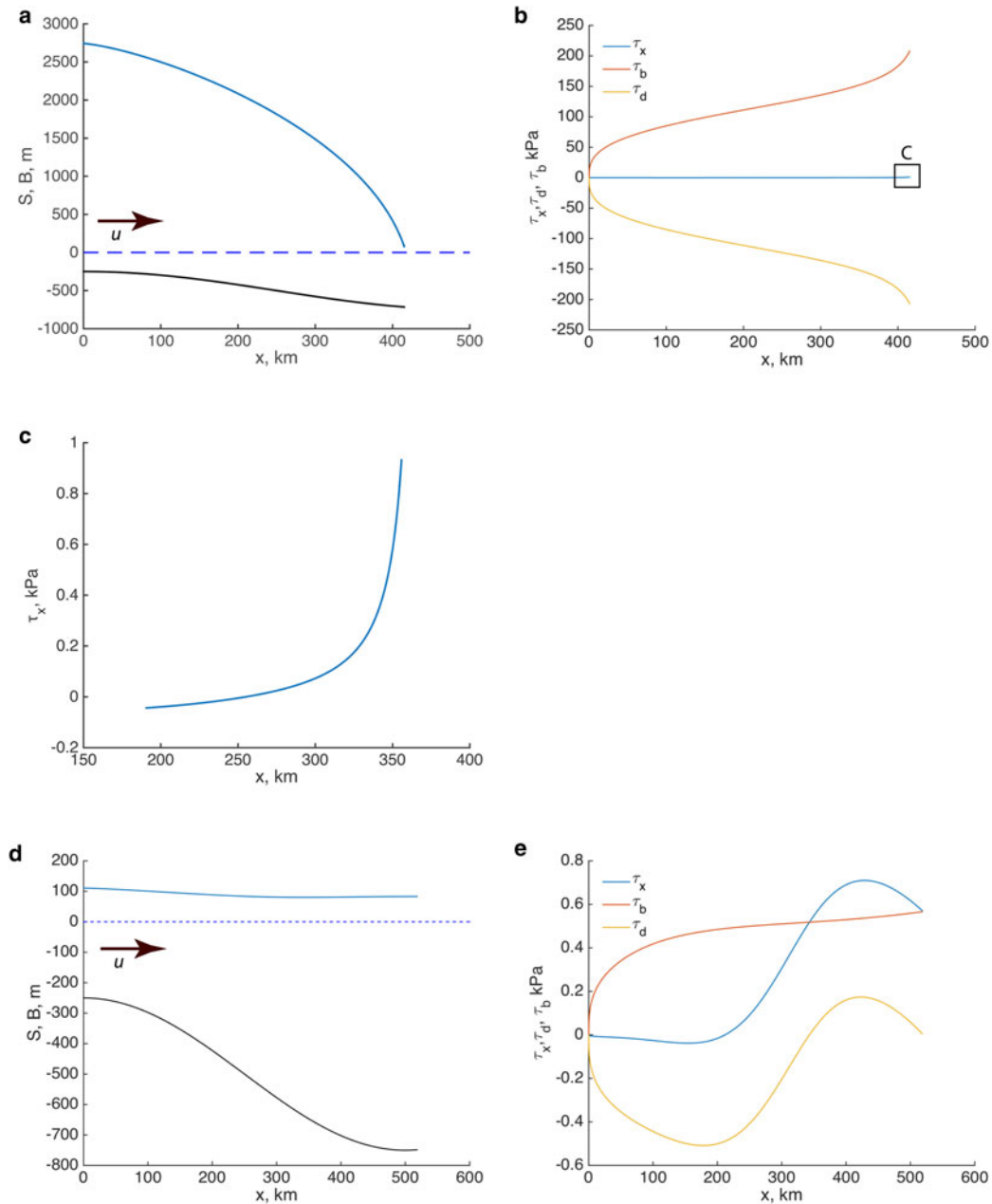


Fig. 3. Surface elevation and components of the momentum balance for a high $C = 7.6 \cdot 10^6 \text{ Pa m}^{-1/3} \text{ s}^{1/3}$ (panels (a)–(c)) and low $C = 7.6 \cdot 10^3 \text{ Pa m}^{-1/3} \text{ s}^{1/3}$ (panels (d)–(e)) values of the sliding coefficient. Panels (a) and (d) surface (s) and bed (b) elevation (m), arrows show the ice-flow direction; (b), (c) and (e) components of the momentum balance, τ_x , τ_b and τ_d (kPa); insets in panel (b) show locations of a zoom shown in panel (c) τ_x for $C = 7.6 \cdot 10^6 \text{ Pa m}^{-1/3} \text{ s}^{1/3}$. The simulation parameters are the following: bed elevation $b(x) = b_0 + b_0 \cos(\pi x/L)$, with $b_0 = -500 \text{ m}$, $b_0 = 250$, and $L = 500 \text{ km}$; ice stiffness parameter $A = 1.35 \cdot 10^{-25} \text{ Pa}^{-3} \text{ s}^{-1}$ (corresponds to $T_{ice} \approx -20^\circ\text{C}$); and accumulation rate $\dot{a} = 0.94 \text{ m a}^{-1}$.

problem (13)–(16) a small parameter δ appears only in the momentum balance (19a). This reduction, which was introduced by Schoof (2007b, Appendix A) in connection with the corresponding problem in which the basal stress is of the same order as the driving stress, is exact: the solution for any pair of values of ϵ and δ may be obtained from the solution of the problem (19) through the scale assignment (17). However if, as we do here, one seeks an approximate solution of the problem (19) as a perturbation series expansion in the small parameter δ , one must formally assign $\delta \sim \epsilon$ if the other terms in (19) are to be $O(1)$.

To illustrate how different scales of basal shear affect the steady-state configurations we solve the problem (1)–(9) numerically (the details of numerical solver and used parameters are described in Appendix A) with two different values of the sliding parameter C . In the first experiment we use the same value as

used by Schoof (2007b) $C = 7.6 \cdot 10^6 \text{ Pa m}^{-1/3} \text{ s}^{1/3}$; in the second experiment, we use the value of C three orders of magnitude smaller $C = 7.6 \cdot 10^3 \text{ Pa m}^{-1/3} \text{ s}^{1/3}$. The computed ice-stream geometry and the momentum balance components for the two cases are markedly different (Fig. 3). In the case of a large value of the sliding coefficient, ice thickness is significantly larger in the interior than the magnitude of the bed elevation throughout the ice stream, and also than the ice thickness in the immediate vicinity of the grounding line. Consequently, the surface gradients are large in the vicinity of the grounding line (Fig. 3a). In contrast, in the case of low value of C , surface elevation neither varies substantially through the length of the ice stream nor in the immediate vicinity of the grounding line (Fig. 3d). Also, the ice thickness has the same order of magnitude as bed elevation, and for the chosen bed geometry, it is larger at the grounding line than in the interior of the ice stream.

The momentum balance in the case of large C (Fig. 3b) is predominantly between the driving and basal stresses. These are of the order of 100–200 kPa throughout the length of the ice stream, and achieve their maximum at the grounding line. Although the divergence of the longitudinal stress increases near the grounding line (Fig. 3c), its magnitude remains significantly (two orders) smaller than the magnitudes of the driving and basal stresses. In the case of low C (Fig. 3e), the driving and basal stresses are much smaller than in the case of large C (less than 1 kPa), and the divergence of the longitudinal stress is of the same order as the basal shear (Fig. 3e), in line with the conclusions of MacAyeal (1989) who found that ‘...basal drag and horizontal deviatoric stress gradients can contribute equally in balancing gravitational driving stress.’ These results suggest that the two regimes of high and low basal and driving stresses are very different; they also suggest that the power-law sliding law is capable of producing low surface gradients and low driving stress not only in the vicinity of the grounding line, but through the length of the ice stream, if the sliding coefficient C is small.

Steady states

In this section, we investigate steady solutions to (19) by setting H_T in (19b) to zero. We treat δ as a small parameter and seek a solution as series expansion in δ , i.e.

$$H \sim H_0 + \delta H_1 + \delta^2 H_2 + \dots \quad (20a)$$

$$U \sim U_0 + \delta U_1 + \delta^2 U_2 + \dots \quad (20b)$$

where the coefficients of powers of δ are supposed of $O(1)$. Substituting H and U into the momentum-balance Eqn (19a), the mass-balance equation

$$(UH)_X = \dot{a} \quad (21)$$

and the boundary conditions (19c)–(19e), and equating the coefficients of each power of δ leads to various orders approximations of the problem (19a), (21) and (19c)–(19e). Detailed descriptions of the zeroth- and first-order solutions are provided in Appendix A. In this section we provide a brief summary.

The zeroth-order problem is

$$H_0(H_0 + B)_X = 0 \quad (22a)$$

$$(U_0 H_0)_X = \dot{a} \quad (22b)$$

$$U_0 = 0, \quad X = 0 \quad (22c)$$

$$(H_0 + B)_X = 0, \quad X = 0 \quad (22d)$$

$$H_0 |U_{0X}|^{(1/n)-1} U_{0X} = \frac{1}{2} H_0^2, \quad X = X_g \quad (22e)$$

$$H_0 = -B, \quad X = X_g. \quad (22f)$$

Its solutions, H_0 and U_0 , are determined from (22a) together with (22f), and (22d)

$$H_0(X) = -B(X) \quad (23a)$$

$$U_0(X) = \frac{\int_0^X \dot{a} dx}{H_0(X)} = \frac{Q}{H_0}, \quad (23b)$$

where $Q = \int_0^X \dot{a} dx$ is ice flux.

Expression (23a) describes a solution in which the stream is neutrally buoyant: the thickness equals the bed depth and the surface elevation is zero. It provides no description of the roles of the divergence of the longitudinal stress and the basal shear stress in determining the position of the grounding line, for which we need to determine the first-order solutions. The zeroth-order solution does, however, provide an important insight. Using (23), the stress condition (22e) can be written as

$$QB_X - \dot{a}B = \left(\frac{1}{2}\right)^n |B|^{n+2}, \quad X = X_g, \quad (24)$$

which provides an expression for the grounding flux. $Q(X_g)$ is not a function of $B(X_g)$ alone, as is the case with a high basal shear stress (Schoof, 2007b), but depends in addition on the basal gradient at the grounding line. This arises because, at this order, the surface is flat, and it is the basal gradient, rather than the surface gradient, that accounts for the ice thickness gradient. We will return to the implications of this observation having first obtained the first-order solutions.

The first-order problem is

$$H_{1X} = \frac{1}{H_0} [(H_0 |U_{0X}|^{(1/n)-1} U_{0X})_X - \Gamma |U_0|^{m-1} U_0] \quad (25a)$$

$$(U_1 H_0 + U_0 H_1)_X = 0 \quad (25b)$$

$$U_1 = 0, \quad X = 0 \quad (25c)$$

$$H_{1X} = 0, \quad X = 0 \quad (25d)$$

$$H_1 |U_{0X}|^{(1/n)-1} U_{0X} + \frac{1}{n} H_0 |U_{0X}|^{(1/n)-1} U_{1X} = H_1 H_0, \quad (25e)$$

$$X = X_g$$

$$H_1 = -B, \quad X = X_g. \quad (25f)$$

All the components of the first-order expressions are determined from the zeroth-order solutions U_0 and H_0 (23). Substitution of these solutions and their derivatives into (25a) gives

$$H_{1X} = \frac{|B|^{-(n+2)/n}}{n} |QB_X - \dot{a}B|^{(1/n)-1} [(2-n)B_X(QB_X - \dot{a}B) - B(QB_{XX} - B\dot{a}_X)] - \Gamma \frac{Q^m}{|B|^{m+1}}. \quad (26)$$

This expression has two terms that are determined by bed properties – its geometry (the first term) and basal shear (the second term). The first term, which includes bed elevation B (note that B is a negative quantity), its slope B_X , and curvature B_{XX} , can be regarded as a form drag, which is the resistance to ice flow that arises due to the shape of the bed (e.g. Schoof, 2002a). The last term of (26) is the basal shear expressed in terms of ice flux

$Q = U_0 H_0$. The fact that the basal shear is an additive term suggests that in the low basal and driving stress regimes, ice flow is less sensitive to a specific form of basal shear ('sliding law') as long as its magnitude is low.

In general (26) is not compatible with (25d), suggesting the presence of a boundary layer at the divide at first order. However, as we have already noted, our interest is not in the details at the divide, and we therefore impose a further constraint that $(n - 2)B_X \dot{a} + B \dot{a}_X = 0$ at $X=0$. This is satisfied if, e.g., the bed elevation and accumulation rate have no gradients at the divide, i.e., $B_X(X=0) = 0$ and $\dot{a}_X(X=0) = 0$.

Taking into account the boundary condition (25c), a solution of (25b) is

$$U_1 = -U_0 \frac{H_1}{H_0}. \tag{27}$$

H_1 is determined by integrating (26) using the flotation condition (25f).

Except for the case $B = \text{const}$, which is of limited interest, (26) cannot be integrated analytically. H_1 is ice surface elevation to leading order. It is determined by the integral of expression (26) that itself depends on only the local bed geometry and basal shear. The surface elevation is a non-local function of these bed properties, and depends on their integral effects through the length of the ice stream.

At this point the zeroth- and first-order solutions are determined for any given location of the junction between an ice stream and ice shelf, but we have yet to determine the position of the grounding line X_g . For this purpose we use the remaining stress boundary condition (19d), and determine the grounding line location through the simultaneous solution of this condition and the momentum and mass-balance solutions in the interior of ice stream.

Combining the zeroth- and first-order stress conditions (22e) and (25e), the flotation conditions, (22f) and (25f), the zeroth-order solutions (23) and the first-order solution for U_1 (27), the stress condition (19d) becomes

$$|QB_X - \dot{a}B|^{(1/n)-1} \left[\left(1 - \frac{\delta}{n}\right) (QB_X - \dot{a}B) - \frac{\delta}{n} Q(H_{1X} + B_X) \right] = \frac{1 + \delta}{2} |B|^{((n+2)/n)}, \quad X = X_g. \tag{28}$$

where H_{1X} is given by (26) evaluated at $X = X_g$. Values of X_g are determined as the roots of (28). It is possible that the choices of the functions B and \dot{a} can produce zero, one or more steady-state locations of the grounding line.

Comparing (28) and (24) one can see that acknowledging the role of the basal shear stress and the form drag further increases the parameters on which the flux at the ground line depends to include the basal curvature and the basal sliding coefficient Γ . The dimensional form of (28) is

$$|qb_x - \dot{a}b|^{(1-n)/n} \left[\left(1 - \frac{\delta}{n}\right) (qb_x - \dot{a}b) - \frac{\delta}{n} q(h_{1x} + b_x) \right] = \rho g' A^{(1/n)} |b|^{(n+2)/n} \frac{1 + \delta}{4}, \quad x = x_g, \tag{29}$$

where

$$h_{1x} = \frac{1}{\rho g' |b|} \left\{ \frac{2A^{-(1/n)}}{n|b|^{1/n}} |qb_x - \dot{a}b|^{(1/n)-1} [(2-n)b_x(qb_x - \dot{a}b) - b(qb_{xx} - b\dot{a}_x)] - C \left(\frac{q}{|b|}\right)^m \right\}, \tag{30}$$

where $b(x) < 0$.

Expression (29) may be compared with the relationship derived for unconfined configurations in a regime with a large magnitude basal shear (Schoof, 2007b)

$$q = \left(\frac{A(\rho g)^{n+1} \delta^n}{4^n C} \right)^{1/(m+1)} \left(\frac{|b|}{1 - \delta} \right)^{(m+n+3)/m+1}, \quad x = x_g, \tag{31}$$

where we have applied the flotation condition on the RHS of (31) so to make it comparable with (29). Equation (29) is considerably more complex than (31), and in particular it depends upon the bed shape, and the accumulation rate and its gradient at the grounding line, in addition to the bed elevation itself. According to these, ice streams with the same bed depth at the grounding line can have different fluxes and vice versa; and the relationship can be a multivalued function. Expression (28) results in an ice flux with a finite magnitude even when the basal shear is zero, in contrast to the infinite flux which is the consequence of (31) as $C \rightarrow 0$.

Comparison of approximate and 'exact' solutions

To assess the behaviors of the zeroth- and first-order solutions, and to compare these with the 'exact' solutions, we compute the grounding line position, and the relationship between flux and thickness at the grounding line, for the sinusoidal bed illustrated in Figure 4a, as the accumulation rate is varied. The grounding line positions for the case of the sliding parameter $C=0$ are shown in Figure 4a, the relationships between ice flux and thickness for various values of the sliding parameter C in Figures 4b and 4c. As Figure 4b shows, the relationship between flux and thickness is not a simple, monotonic curve. In this case, for a given flux, steady states can be found at two thicknesses, or for a given thickness, steady states can be found for two values of flux. As C increases, the relative importance of form drag and basal shear changes, and the difference between multiple values decreases. Figures 4a and 4b show solutions obtained from the zeroth- and first-order solutions. The multivalued behavior is qualitatively captured in the zeroth-order solution (black asterisks), although the addition of the role of form drag, which is accounted for when the first-order solution is included and $C = 0$, and the basal shear stress as C increases are quantitatively different. The quantitative difference is apparent too in the grounding line locations. Figure 4a shows three examples of the grounding line positions computed from the zeroth-order expression (24) (black asterisks labeled '1-3'). These positions are substantially different from the 'exact' positions and approximate ones computed using the first-order solutions (filled blue circles and diamonds labeled '1-3').

Figures 4a and 4b also include a comparison with the 'exact' solutions (denoted by circles). These show a good agreement between the 'exact' results and expression (29). This close coincidence indicates that the scale assignment of δ provides a description that closely resembles the actual dynamics. That accurate solutions require a solution to $O(\delta)$ reflects the fact

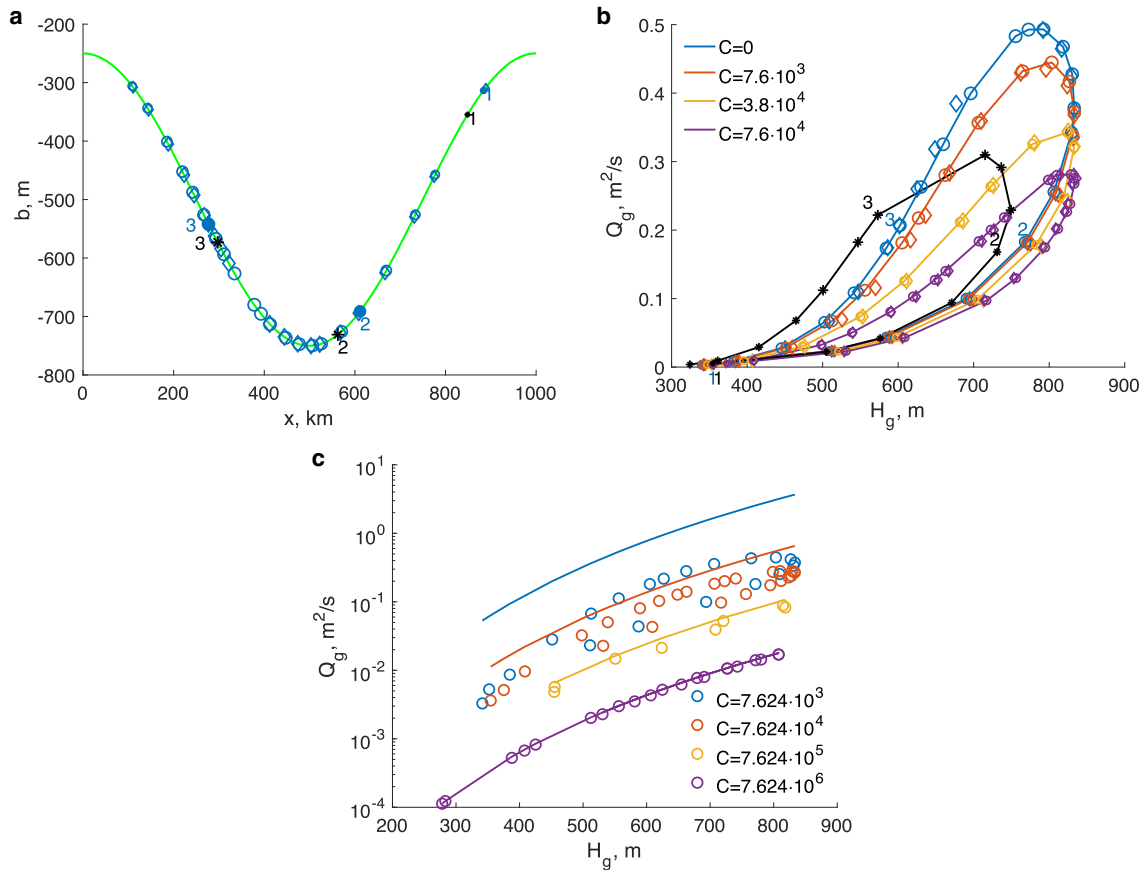


Fig. 4. Conditions at the grounding line. (a) The grounding line position for sliding parameter $C=0$ and discrete values of the accumulation rate \dot{a} ; (b) and (c) the relationship between ice flux and ice thickness computed for various values of the accumulation rate \dot{a} and sliding parameter C . The values of \dot{a} are discretely chosen, ranging from 0.18 to 39.8 m a⁻¹. The size of symbols in panels (a) and (b) correspond to the values of \dot{a} . In panels (a) and (b) circles are ‘exact’ computations, diamonds are the roots of expression (29), asterisks are the roots of the zero-order expression (24). In panel (a) black asterisks with black labels ‘1–3’ are three examples of the roots of the zeroth-order expression (24); filled symbols with blue labels ‘1–3’ are the roots of expression (29) with the same values of \dot{a} as those denoted by black asterisks. The labels ‘1–3’ in panel (b) correspond to the labeled grounding line locations in panel (a). Circles in panel (c) are ‘exact’ solutions and solid lines are the boundary layer relationship (31) derived by Schoof (2007b). Notice logarithmic scale on the vertical axis on panel (c). The bed elevation $b(x)$ has the same analytic form and stiffness parameter A has the same value as those in Figure 3. In all experiments the ice flow is from left to right.

that the value of δ is 0.1. This numerical value is material, in that accurate solutions then need to account for the form drag, and the basal shear if it is present. In detail, there are values of accumulation rate for which the zeroth- and first-order solutions do not provide a solution for a steady-state grounding line, although the ‘exact’ solutions do provide one. These are indicated by fewer diamond and asterisk symbols indicating the approximate and zero-order solutions compared to the circle symbols indicating the ‘exact’ solutions in Figures 4a and 4b.

Figure 4c extends the range of 4b to allow a comparison for values of C of which the basal shear stress is much larger than the contribution of form drag. It shows that the effects of form drag are completely suppressed and the flux–thickness relationship follows expression (31) (purple line in Fig. 4c). On the other hand, for smaller values of C expression (31) consistently overestimates ice flux (and, as we have noted, results in infinity if the basal shear is zero). (Because (29) is not applicable for high values of C , in Figure 4c we have used ‘exact’ solutions for consistency.)

In circumstances where the basal shear is small, the surface slopes and driving stress are determined by the gradient of the longitudinal stress τ_x (the first term on the RHS of (25a) and (30)), which in turn is determined by the ice stiffness parameter A and spatial variability of the bed elevation. Gudmundsson (2003) and Sergienko (2012) show that the effects of the variability in bed elevation on ice flow increase as the basal shear decreases. Figure 5 illustrates the effects of form drag on ice-stream flow. It shows

the analytical (blue curves in panels 5a–5b and 5d–5e) and ‘exact’ solutions (red curves in panels 5a–5b and 5d–5e) with the sliding parameter $C=0$ for two bed elevations that have the same slope, but one of which has low-amplitude long-period (more than 10 ice thicknesses) undulations $b(x) = b_0 + b_x x + b_a \sin(\pi x/L)$ where $b_0 = -100$ m, $b_x = -0.0005$, $b_a = 5$ m, and $L=5$ km (Figs 5a–5c) and whereas the second one does not $b(x) = b_0 + b_x x$, where $b_0 = -200$ m, $b_x = -0.0005$ (Figs 5d–5f). The configurations of the two ice streams are significantly different: the grounding line position in the case of the bed with undulations is ~ 116 km upstream of the grounding line position in the case of the bed without undulations; the maximum ice flow speed is 26% slower in the former case than in the latter case; the maximum magnitude of the divergence of the longitudinal stress (and consequently driving stress) is more than two orders of magnitude larger in the former case than in the latter, although it is noticeable that the surface elevation in both cases is very similar. When the basal shear stress is low, the detailed shape of the bed has a strong influence on the location of the grounding line.

Linear stability analysis of steady states

The conclusion that a grounding line is unconditionally unstable if the bed slope is retrograde, due to Weertman (1974) and given a more precise form by Schoof (2012), depends on the result (31) that the grounding line flux is a monotonically increasing function of the depth of the bed. However, as our results show, this

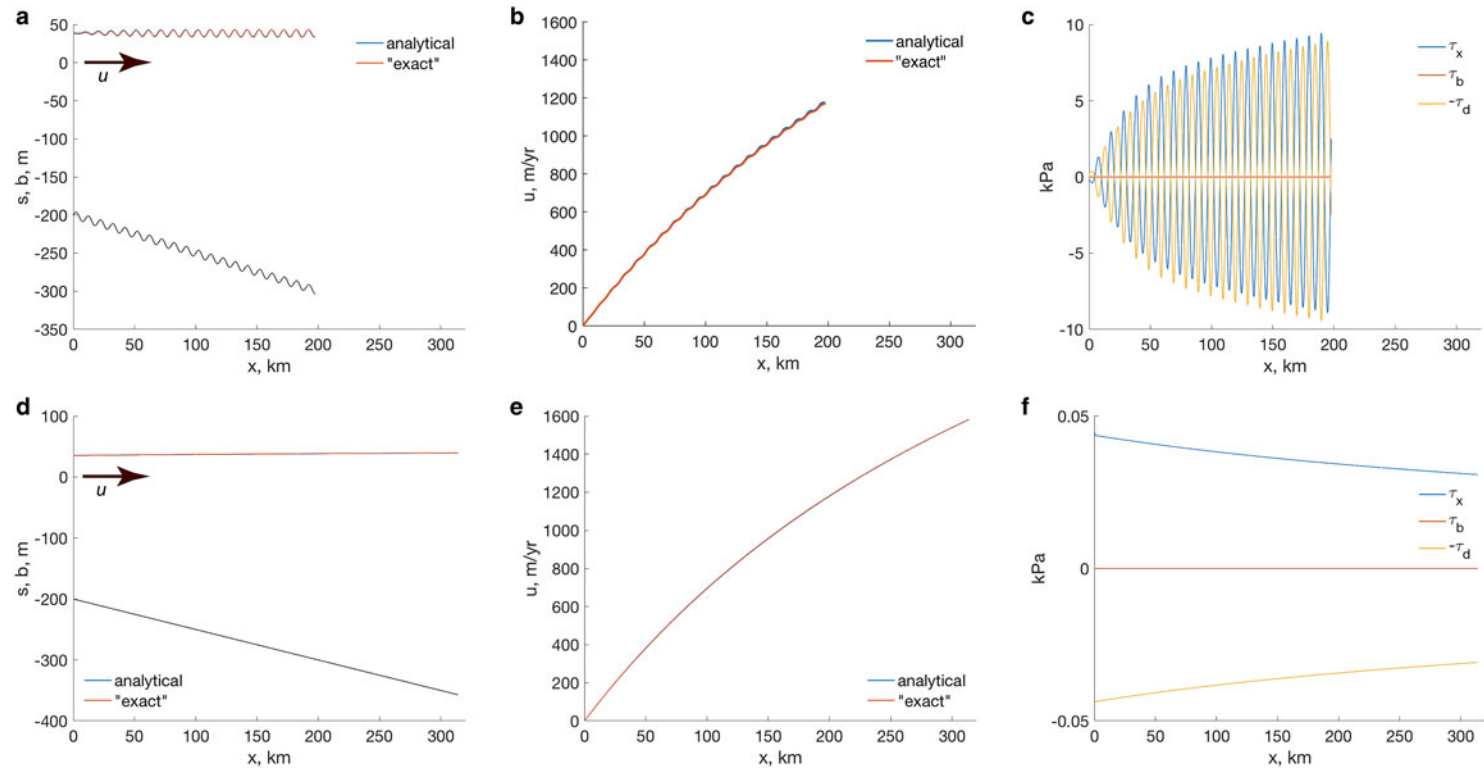


Fig. 5. Effects of form drag. Steady-state configurations computed with $C=0$ for two bed elevation profiles: $b(x) = b_0 + b_x x + b_0 \sin(\pi x/L)$ panels (a)–(c) and $b(x) = b_0 + b_x x$ panels (d)–(f). (a) and (d) profiles of surface and bed elevation, arrows show the ice-flow direction; (b) and (e) ice velocity; (c) and (f) the momentum-balance components. The terms of the momentum-balance (panels (c) and (f)) computed numerically. Note that panels (c) and (f) show $-\tau_d$.

result holds only when the basal shear and driving stress have large magnitudes. When the driving and basal shear stresses are small, the flux–thickness relationship (29) explicitly depends on the basal slope b_x and curvature b_{xx} , the accumulation rate \dot{a} and its gradient \dot{a}_x , the basal shear stress, and the exponent n of the ice rheology ($n > 2$ or $n \leq 2$). Their various combinations could equally result in an increase or decrease in the ice flux with increase in ice thickness. One might anticipate that the stability of the grounding line position may exhibit a similar complexity.

To investigate the stability of the steady-state grounding line positions, we consider a time-variant problem with small deviations from a steady-state configuration, i.e.,

$$H = H_{ss}(X) + \sigma \tilde{H}(X, T), \quad (32a)$$

$$U = U_{ss}(X) + \sigma \tilde{U}(X, T), \quad (32b)$$

$$X_g = X_{gss} + \sigma \tilde{X}_g(T) \quad (32c)$$

where σ is a small perturbation parameter and H_{ss} , U_{ss} and X_{gss} are the solutions of (19a), (21) and (19c)–(19e). Substituting these expressions into the momentum, mass-balance equations and the boundary conditions and collecting the terms of $O(\sigma)$ yields the following perturbation problem

$$\delta \left[\tilde{H} |U_{ssX}|^{(1/n)-1} U_{ssX} + \frac{1}{n} H_{ss} |U_{ssX}|^{(1/n)-1} \tilde{U}_X \right]_X - \tilde{H}_X H_{ss} - \tilde{H} (H_{ss} + B)_X - m \delta \Gamma |U_{ss}|^{m-1} \tilde{U} = 0 \quad (33a)$$

$$\tilde{H}_T + (\tilde{U} H_{ss} + \tilde{H} U_{ss})_X = 0 \quad (33b)$$

$$\tilde{H}_X = \tilde{U} = 0, \quad X = 0 \quad (33c)$$

$$\frac{1}{n} H_{ss} |U_{ssX}|^{(1/n)-1} \tilde{U}_X + (H_{ss} |U_{ssX}|^{(1/n)-1} U_{ssX})_X \tilde{X}_g =$$

$$H_{ss} \left(H_{ssX} \tilde{X}_g + \frac{1}{2} \tilde{H} \right), \quad X = X_{gss} \quad (33d)$$

$$\tilde{H} + H_{ssX} \tilde{X}_g = -\frac{B_X}{1-\delta} \tilde{X}_g, \quad X = X_{gss}. \quad (33e)$$

As in the previous section, we use the method of perturbation series expansion to construct to $O(\delta)$ solutions of (33). This is algebraically quite complex, and we give the details in Appendix B. However, the form of the solution for \tilde{X}_g is quite simple. It is,

$$\tilde{X}_g \simeq -\frac{\tilde{H}(0)}{H_{ss1X} + B_X} e^{\Lambda T} \quad (34)$$

where $\tilde{H}(0)$ is a small initial perturbation, and the denominator is evaluated at X_{gss} . As is apparent from this form, the stability of the steady state is entirely determined by the sign of a parameter Λ in (34). For $\Lambda < 0$, they are stable and for $\Lambda > 0$ they are unstable. This

parameter is given by

$$\Lambda = (B_X X_{gss} - B)^{-1} \left\{ \dot{a} - \left(\frac{2}{n} - 1 \right) \frac{Q_{gss}}{B} B_X + \left(3n - \frac{2}{n} + 3 \right) \frac{B_X (Q_{gss} B_X - B \dot{a})}{B (H_{ss1X} + B_X)} + \left(\frac{1}{n} - 1 \right) Q_{gss} \frac{Q_{gss} B_{XX} - B \dot{a}_X}{Q_{gss} B_X - B \dot{a}} + \frac{1}{H_{ss1X} + B_X} \times \left[Q_{gss} \left(\frac{1}{n} B_{XX} + H_{ss1XX} \right) - \left(\frac{1}{n} - 1 \right) B \dot{a}_X \right] \right\} \quad (35)$$

and is a function of the steady-state parameters taken at $X = X_{gss}$. In dimensional terms Λ is

$$\Lambda = (b_x x_g - b)^{-1} \left\{ \dot{a} - \left(\frac{2}{n} - 1 \right) \frac{q}{b} b_x + \left(3n - \frac{2}{n} + 3 \right) \times \frac{b_x (q b_x - b \dot{a})}{b (\delta h_{1x} + b_x)} + \left(\frac{1}{n} - 1 \right) q \frac{q b_{xx} - b \dot{a}_x}{q b_x - b \dot{a}} + \frac{1}{n (\delta h_{1x} + b_x)} \left[q (\delta n h_{1xx} + b_{xx}) + (n - 1) b \dot{a}_x \right] \right\} \quad (36)$$

where h_{1x} is defined by (30).

As we surmised, the stability condition in the low stress regime depends in a complex way on the accumulation and basal geometry. In the low-driving and basal stress regime, stability is determined by a combination of the bed geometry – its slope b_x and curvature b_{xx} – the accumulation rate \dot{a} and its gradient \dot{a}_x ; it also implicitly depends on the basal shear τ_b and its gradient through h_{1x} and h_{1xx} terms. Figure 6a illustrates the stability condition $\Lambda < 0$ for the case of bed elevation shown in Figure 4a and the sliding parameter $C = 1.8 \cdot 10^4 \text{ Pa m}^{-1/3} \text{ s}^{1/3}$. The grounding line can be both stable (open circles) and unstable (crossed circles) at locations with positive and negative bed slopes.

To validate the stability condition, which is derived based on approximations of the perturbation theory, we obtain the ‘exact’ solutions by solving the time-dependent problem (1)–(10) numerically for an ice stream whose grounding line is perturbed from its steady state. These simulations are performed for the configurations with the steady-state grounding line positions marked by triangles in Figure 6a. In both simulations, at $t = 0$ the grounding line position is displaced 1 km upstream of its steady-state position and the steady-state ice thickness and velocity are used as initial conditions. Figure 6b illustrates the grounding line behavior perturbed from an unstable position. After initial advance toward the steady-state position, the grounding line retreats away from it with the distance increasing exponentially in time ($\Lambda > 0$). In contrast, the grounding line perturbed from the stable position (Fig. 6c) advances beyond its steady-state position and then retreats to it with the distance decreasing exponentially in time ($\Lambda < 0$) and stabilizes at its steady-state location. In performing these ‘exact’ time-dependent simulations, we have found consistently that they contain the initial transients illustrated in Figures 6b–6c that are not accounted for in the linearized theory that leads to (34). However, we have also found, consistently, that the sign of Λ determined from (36) correctly determines the stability, and that, following the transient, the value of Λ determined from (36) correctly describes the time-dependent solutions. Due to the presence of the transients in the ‘exact’ solutions, the exponential functions illustrated

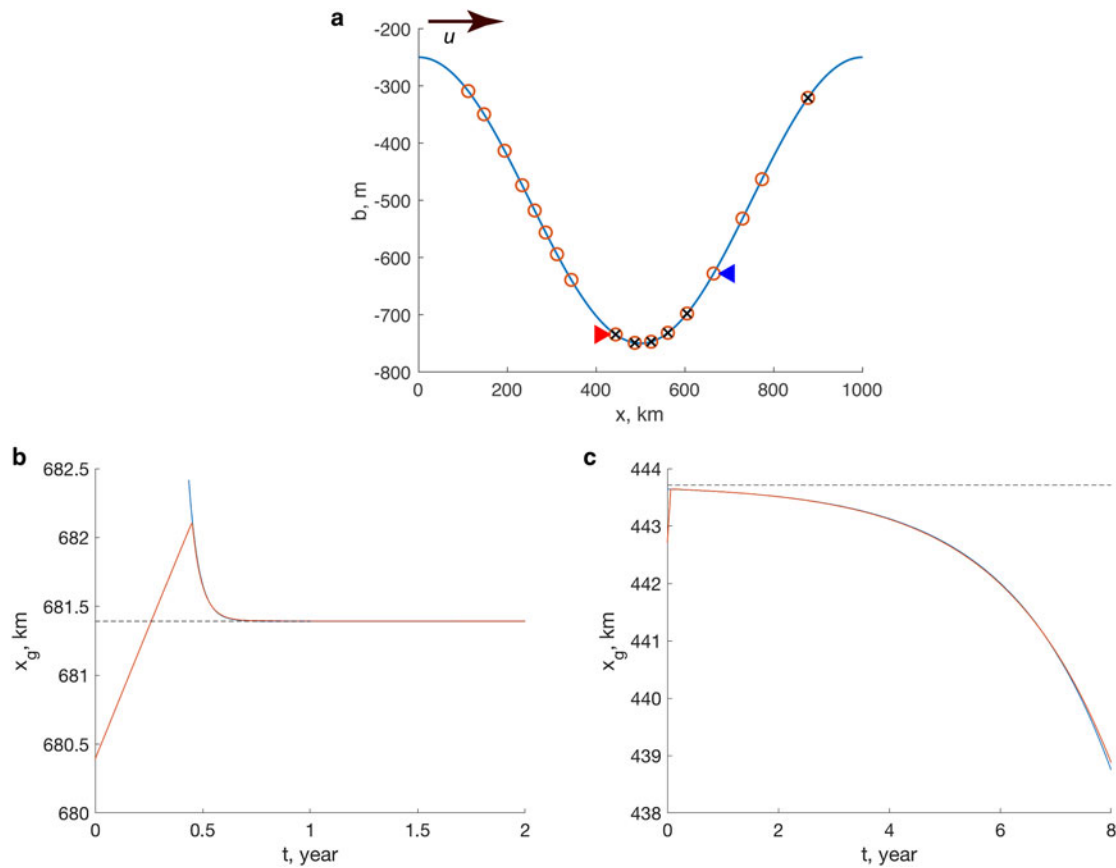


Fig. 6. Stability condition. (a) Bed elevation and steady-state grounding line positions for $C = 1.8 \cdot 10^4 \text{ Pa m}^{-1/3} \text{ s}^{1/3}$ and different discrete values of the accumulation rate \dot{a} ; stable positions are open circles, unstable positions are crossed circles. (b) Time evolution of the grounding line marked by a red triangle in panel (a) perturbed from its steady state; (c) same as (b) for a position marked by blue triangle. In panels (b) and (c) red lines are numerical solutions; blue lines are fitting curves $\sim e^{\Lambda t}$, where Λ is computed using expression (36); dashed lines indicate steady-state positions marked by triangles in panel (a).

in Figures 6b–6c are fit to the form $\tilde{X}_{g0} e^{\Lambda(t-t_0)}$ (where X_{g0} and t_0 are fitting constants), with Λ determined from (36).

This behavior is quite distinct from that associated with high basal and driving stresses. The expression (36) can be compared with the stability criterion for the large basal and driving stress regimes, which is $q'(h(x_g, \dot{a}(x_g))) > \dot{a}$ (Schoof, 2012), which cannot be satisfied on retrograde beds. In contrast, the stability of the two configurations illustrated in Figures 6b–6c is the reverse. The grounding line position on the prograde bed (6b) is unstable; that on the retrograde bed (6c) is stable.

Equation (34) shows that the reciprocal of the parameter Λ , $t_e = |\Lambda|^{-1}$ is the e -folding time of adjustment of a marine ice sheet perturbed from its steady-state configuration. In contrast to the case of high basal stress, in which only the sign of Λ can be inferred (Schoof, 2012), (36) provides an expression for the magnitude of this constant, and it is of some interest to consider the magnitude of these. Figure 7 shows t_e as the sliding parameter C and the accumulation rate \dot{a} are varied. The values of t_e vary from months to hundreds of years. These values provide, in any given case, some insight into the extent to which the stability analysis has value in considering the evolution of the sheet independently of variations in external forcing. At the lower end, which is short in comparison with variations of climate (parameterized here through the accumulation rate \dot{a} and implicitly through the temperature-dependent ice-stiffness parameter Λ) or sea level, one may expect the sheet to exhibit stable or unstable behavior as identified by the stability analysis; at the upper end, an observed variation in the position of the grounding line may reflect the variations in climate or sea level and have little to do with any internal instability associated with its configuration.

Discussion and conclusions

Motivated by the present-day Siple Coast ice streams characterized by low surface slopes and consequently driving stress, we focused this study on the grounding line dynamics of unconfined marine ice sheets with grounded ice streams in a regime of low driving and basal stresses. Using the perturbation series expansion method, we have constructed analytic expressions for various approximation orders of the ice-stream thickness, velocity and flux. Our analysis suggests that the dynamics of such marine ice sheets is markedly different from those with ice streams experiencing high driving and basal stresses, configurations extensively studied previously (Weertman, 1974; Schoof, 2007b, 2012; Tsai and others, 2015). Our results demonstrate that in circumstances where the basal shear is low or absent through the length of the ice stream, there is no boundary layer in the vicinity of the grounding line as in the regime of high driving and basal stresses. The approximate expressions for ice thickness show that low surface slopes and the driving stress are a consequence of low or absent basal shear (at the zeroth-order the former are zero), and they increase in response to increase of the magnitude of the basal shear. Therefore, observed low surface slopes on the present-day ice stream are indicative of low basal shear.

In contrast to the high driving-stress regime in which the effects of the longitudinal stress divergence are small, in the low driving-stress regime, its magnitude can be of the same order as the other components of the ice-stream momentum balance. In circumstances where the basal shear is zero, the longitudinal stress divergence balances the driving stress at higher orders. Its magnitude increases with increasing spatial variability of the underlying

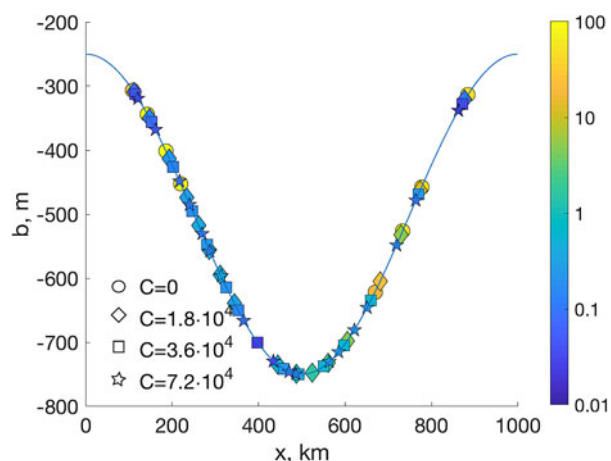


Fig. 7. e -folding time (years) of all grounding line positions shown in Figure 4b.

bed geometry. The longitudinal stress divergence can be viewed as form drag that together with basal shear (when it is non-zero) inhibits ice flow (e.g. Schoof, 2002a; Gudmundsson, 2003; Sergienko, 2012). Low-amplitude bed undulations (on the order of a few meters) can result in form drag on the order of a few kPa (Figs 5a–c). This has the direct consequence that bed elevation measurements, which are presently accurate to 30–100 m, (Fretwell and others, 2013), are insufficient to accurately determine the form drag, and also suggests that the accuracy of the surface observations used to constrain bed elevation based on mass-conservation principles (e.g. Morlighem and others, 2017) may not be sufficient to resolve small amplitude bed topography.

The importance of the shape of the bed and its slope manifests itself in the functional dependence of ice flux on ice thickness at the grounding line (Eqns (24), (28) and (29)): it is no longer a single-valued monotonic function as in the high driving stress regime (31), and depending on the bed geometry and the accumulation rate, ice streams can have the same flux through the grounding line with significantly different ice thicknesses (Fig. 4). Our results show that in the low driving stress regime, the ice flux at the grounding line is consistently lower than predicted by expression (31), and is finite in the case of the zero basal shear, in contrast to the infinite flux according to (31). These results suggest that ice-sheet models that employ (31) relationship to parameterize the grounding line dynamics (e.g., Pollard and DeConto, 2009) consistently overestimate the ice flux through the grounding line for ice streams with low driving and basal stress. Such models are also prone to unstoppable grounding line migration, which is an explicit consequence of the use of (31).

Linear stability analysis of steady-state configurations (section ‘Linear stability analysis of steady states’) suggests that in the low driving and basal stress regime, unconfined marine ice sheets do not conform exactly to the marine ice-sheet instability hypothesis, according to which marine ice sheets with grounding lines on beds with retrograde slopes (the bed elevation increases in the direction of ice flow) are always unconditionally unstable (Weertman, 1974; Schoof, 2007b, 2012). Instead, in the regime studied here, the grounding line stability is determined by a combination of form drag (i.e., the geometric bed properties – elevation, slopes and curvature), basal shear and the accumulation rate and their gradients (Eqns (35) and (36)). These results demonstrate that the bed slope alone is not a sufficient indicator of the marine ice-sheet stability (Fig. 6).

The results of our linear-stability analysis have direct application to present-day ice sheets, despite being derived for highly simplified and idealized configurations. In the low basal stress

regime, we are able to calculate the magnitude, in addition to the sign, of the e -folding time of the ice sheet in response to a small perturbation. Our analysis shows that in the low driving and basal stress regime the e -folding time can range from months to hundreds of years, depending on the bed properties (its geometry and basal shear), accumulation, its gradients and its higher spatial derivatives (Fig. 7). At the low end of this range, sub-monthly timescales are significantly shorter than those of climate or sea level variability. Conversely, with e -folding times of some hundreds of years or longer, an observed grounding line variation may result entirely from externally-forced changes (e.g., Fyke and others, 2018). This leads us to the view that care is needed, in considering the cause of grounding line retreat such as that presently observed in West Antarctica, to distinguish the effects of external forcing from those of a configurational instability.

Acknowledgments. We would like to thank Scientific Editor Jonathan Kingslake and two anonymous referees for thoughtful comments and useful suggestions that greatly improved the manuscript. OS is supported by awards NA08OAR4320752 and NA13OAR439 from the National Oceanic and Atmospheric Administration, US Department of Commerce. The statements, findings, conclusions and recommendations are those of the authors and do not necessarily reflect the views of the National Oceanic and Atmospheric Administration, or the US Department of Commerce.

References

- Chugunov V and Wilchinsky A (1996) Modeling of a marine glacier and ice-sheet/ice-shelf transition zone based on asymptotic analysis. *Annals of Glaciology* **23**, 59–67.
- Comsol (2018) *Reference Manual*. Boston, MA: COMSOL.
- Engelhardt H, Humphrey N, Kamb B and Fahnestock F (1990) Physical conditions at the base of a fast moving Antarctic ice stream. *Science* **248** (4951), 57–59.
- Favier L, Pattyn F, Berger S and Drews R (2016) Dynamic influence of pinning points on marine ice-sheet stability: a numerical study in Dronning Maud Land, East Antarctica. *The Cryosphere* **10**(6), 2623–2635. doi: 10.5194/tc-10-2623-2016.
- Fowler AC (1992) Modelling ice sheet dynamics. *Geophysical and Astrophysical Fluid Dynamics* **63**, 29–65.
- Fretwell P and 57 others (2013) Bedmap2: improved ice bed, surface and thickness datasets for Antarctica. *The Cryosphere* **7**, 375–393. doi: 10.5194/tc-7-375-2013.
- Fyke J, Sergienko O, Löfveström M, Price S and Lenaerts JTM (2018) An overview of interactions and feedbacks between ice sheets and the earth system. *Reviews of Geophysics* **56**(2), 361–408. doi: 10.1029/2018RG000600.
- Gudmundsson GH (2003) Transmission of basal variability to a glacier surface. *Journal of Geophysical Research* **108**(B5), 1–19. doi: 10.1029/2002JB002107.
- Haran T, Bohlander J, Scambos T and Fahnestock M (2005) *MODIS Mosaic of Antarctica (MOA) Image Map*. Boulder, CO, USA: National Snow and Ice Data Center. doi: 10.7265/N5ZK5DM5, digital media.
- Haseloff M and Sergienko OV (2018) The effect of buttressing on grounding line dynamics. *Journal of Glaciology* **64**(245), 417–431. doi: 10.1017/jog.2018.30.
- Joughin I, MacAyeal D and Tulaczyk S (2004) Basal shear stress of the Ross ice streams from control method inversions. *Journal of Geophysical Research* **109**, 1–20. doi: 10.1029/2003JB002960.
- MacAyeal DR (1989) Large-scale ice flow over a viscous basal sediment – theory and application to Ice Stream B, Antarctica. *Journal of Geophysical Research* **94**(B4), 4071–4087.
- MacAyeal DR (1992) The basal stress-distribution of Ice Stream E, Antarctica, inferred by control methods. *Journal of Geophysical Research* **97**(B1), 595–603.
- MacAyeal DR and Barcilon V (1988) Ice-shelf response to ice-stream discharge fluctuations: I. Unconfined ice tongues. *Journal of Glaciology* **34** (116), 121–127.
- MacAyeal DR, Bindshadler RA and Scambos TA (1995) Basal friction of Ice Stream E, West Antarctica. *Journal of Glaciology* **41**(138), 247–262.
- Morlighem M and 31 others (2017) Bedmachine v3: complete bed topography and ocean bathymetry mapping of Greenland from multibeam

- echo sounding combined with mass conservation. *Geophysical Research Letters* **44**(21), 11051–11061. doi: 10.1002/2017GL074954.
- Nowicki SM and Wingham DJ** (2008) Conditions for a steady ice sheet-ice shelf junction. *Earth and Planetary Science Letters* **265**, 246–255.
- Pollard D and DeConto RM** (2009) Modelling West Antarctic Ice Sheet growth and collapse through the past five million years. *Nature* **458** (7236), 329–333. doi: 10.1038/nature07809.
- Rose K** (1979) Characteristics of ice flow in Marie Byrd Land, Antarctica. *Journal of Glaciology* **24**(90), 63–76.
- Schäfer M and Turek S** (1996) Benchmark computations of laminar flow around cylinder. In Hirschel EH (ed.), *Flow Simulation with High-Performance Computers II*, vol. 52 Notes on Numerical Fluid Mechanics. Berlin: Springer, pp. 547–556.
- Schoof C** (2002a) Basal perturbations under ice streams: form drag and surface expression. *Journal of Glaciology* **48**(162), 407–416.
- Schoof C** (2007b) Ice sheet grounding line dynamics: steady states, stability, and hysteresis. *Journal of Geophysical Research* **112**, F03S28. doi: 10.1029/2006JF000664.
- Schoof C** (2007b) Marine ice-sheet dynamics. Part 1. The case of rapid sliding. *Journal of Fluid Mechanics* **573**, 27–55. doi: 10.1017/S0022112006003570.
- Schoof C** (2012) Marine ice sheet stability. *Journal of Fluid Mechanics* **698**, 62–72. doi: 10.1017/jfm.2012.43.
- Sergienko OV** (2012) The effects of transverse bed topography variations in ice-flow models. *Journal of Geophysical Research* **117**, F03011. doi: 10.1029/2011JF002203.
- Sergienko OV and Hindmarsh RCA** (2013) Regular patterns in frictional resistance of ice-stream beds seen by surface data inversion. *Science* **342** (6162), 1086–1089. doi: 10.1126/science.1243903.
- Sergienko OV, Bindschadler RA, Vornberger PL and MacAyeal DR** (2008) Ice stream basal conditions from block-wise surface data inversion and simple regression models of ice stream flow: application to Bindschadler Ice Stream. *Journal of Geophysical Research* **113**, 1–11. doi: 10.1029/2008JF001004.
- Sergienko OV, Creyts TT and Hindmarsh RCA** (2014) Similarity of organized patterns in driving and basal stresses of Antarctic and Greenland ice sheets beneath extensive areas of basal sliding. *Geophysical Research Letters* **41**(11), 3925–3932. doi: 10.1002/2014GL059976.
- Tsai VC, Stewart AL and Thompson AF** (2015) Marine ice-sheet profiles and stability under Coulomb basal conditions. *Journal of Glaciology* **61**(226), 205–215.
- Weertman J** (1974) Stability of the junction of an ice sheet and an ice shelf. *Journal of Glaciology* **13**(67), 3–11.
- Wilchinsky A** (2009) Linear stability analysis of an ice sheet interacting with the ocean. *Journal of Glaciology* **55**(89), 13–20.

Appendix A. Steady-state problem

Here we describe the zeroth and first orders of the steady-state problem (19a), (21) and (19c)–(19e) and their solutions. First, we construct solutions of the zeroth-order problem and express them through the external parameters of the problem (e.g., the accumulation rate, bed elevation). Next, we use the zeroth-order solutions to construct the first-order solutions. Substituting the zeroth- and first-order solutions to expression (19d) we derive an implicit condition for the location of the grounding line X_g . The same expression represents a functional relationship between the ice flux and thickness at the grounding line. All expressions derived here are non-dimensional. The dimensional forms are listed in section ‘Steady states’ of the main text.

The zeroth-order problem is

$$H_0(H_0 + B)_X = 0 \quad (\text{A1a})$$

$$(U_0 H_0)_X = \dot{a} \quad (\text{A1b})$$

$$U_0 = 0, \quad X = 0 \quad (\text{A1c})$$

$$(H_0 + B)_X = 0, \quad X = 0 \quad (\text{A1d})$$

$$H_0 |U_{0X}|^{(1/n)-1} U_{0X} = \frac{1}{2} H_0^2, \quad X = X_g \quad (\text{A1e})$$

$$H_0 = -B, \quad X = X_g. \quad (\text{A1f})$$

Its solutions, H_0 and U_0 , are determined from (A1a) and (A1b)

$$H_0(X) = -B(X) \quad (\text{A2a})$$

$$U_0(X) = \frac{\int_0^X \dot{a} dx}{H_0(X)} = \frac{Q}{H_0}, \quad (\text{A2b})$$

where $Q = \int_0^X \dot{a} dx$. Using

$$U_{0X} = \frac{Q_X}{H_0} - Q \frac{H_{0X}}{H_0^2} = \frac{\dot{a}}{H_0} - Q \frac{H_{0X}}{H_0^2}. \quad (\text{A3})$$

The stress condition at the grounding line (A1e) can be written as

$$\dot{a} H_0 - Q H_{0X} = \left(\frac{1}{2}\right)^n H_0^{n+2}, \quad X = X_g \quad (\text{A4})$$

This expression represents the zeroth-order relationship between the ice flux and ice thickness at the grounding line. It does not depend on Γ , and consequently the grounding line positions determined as roots of this expression are the same for any values of sliding. The first-order problem is

$$H_{1X} = \frac{1}{H_0} \left[(H_0 |U_{0X}|^{(1/n)-1} U_{0X})_X - \Gamma |U_0|^{m-1} U_0 \right] \quad (\text{A5a})$$

$$U_1 = -U_0 \frac{H_1}{H_0} \quad (\text{A5b})$$

$$U_1 = 0, \quad X = 0 \quad (\text{A5c})$$

$$H_1 |U_{0X}|^{(1/n)-1} U_{0X} + \frac{1}{n} H_0 |U_{0X}|^{(1/n)-1} U_{1X} = H_1 H_0, \quad X = X_g \quad (\text{A5d})$$

$$H_1 = -B, \quad X = X_g. \quad (\text{A5e})$$

Expression for U_{1X} is determined by differentiating (A5b)

$$U_{1X} = -U_{0X} \frac{H_1}{H_0} + U_0 \frac{H_{0X} H_1}{H_0^2} - U_0 \frac{H_{1X}}{H_0} \quad (\text{A6})$$

and accounting for the flotation condition, (22f) and (A5e), this expression at $X = X_g$ is

$$U_{1X}(X_g) = -U_{0X} + U_0 \frac{H_{0X}}{H_0} - U_0 \frac{H_{1X}}{H_0}. \quad (\text{A7})$$

We note that all components of the above expression are determined from the zeroth-order solutions U_0 and H_0 (A2). Thus,

$$U_{0X} = \frac{Q_X}{H_0} - Q \frac{H_{0X}}{H_0^2} = \frac{\dot{a}}{H_0} - Q \frac{H_{0X}}{H_0^2} \quad (\text{A8})$$

where $Q_X = \dot{a}$ was taken into account.

The expression for $H_0 |U_{0X}|^{(1/n)-1} U_{0X}$ can be written as

$$H_0 |U_{0X}|^{(1/n)-1} U_{0X} = \left| \dot{a} H_0^{n-1} - H_0^{n-2} Q H_{0X} \right|^{(1/n)-1} (\dot{a} H_0^{n-1} - H_0^{n-2} Q H_{0X}), \quad (\text{A9})$$

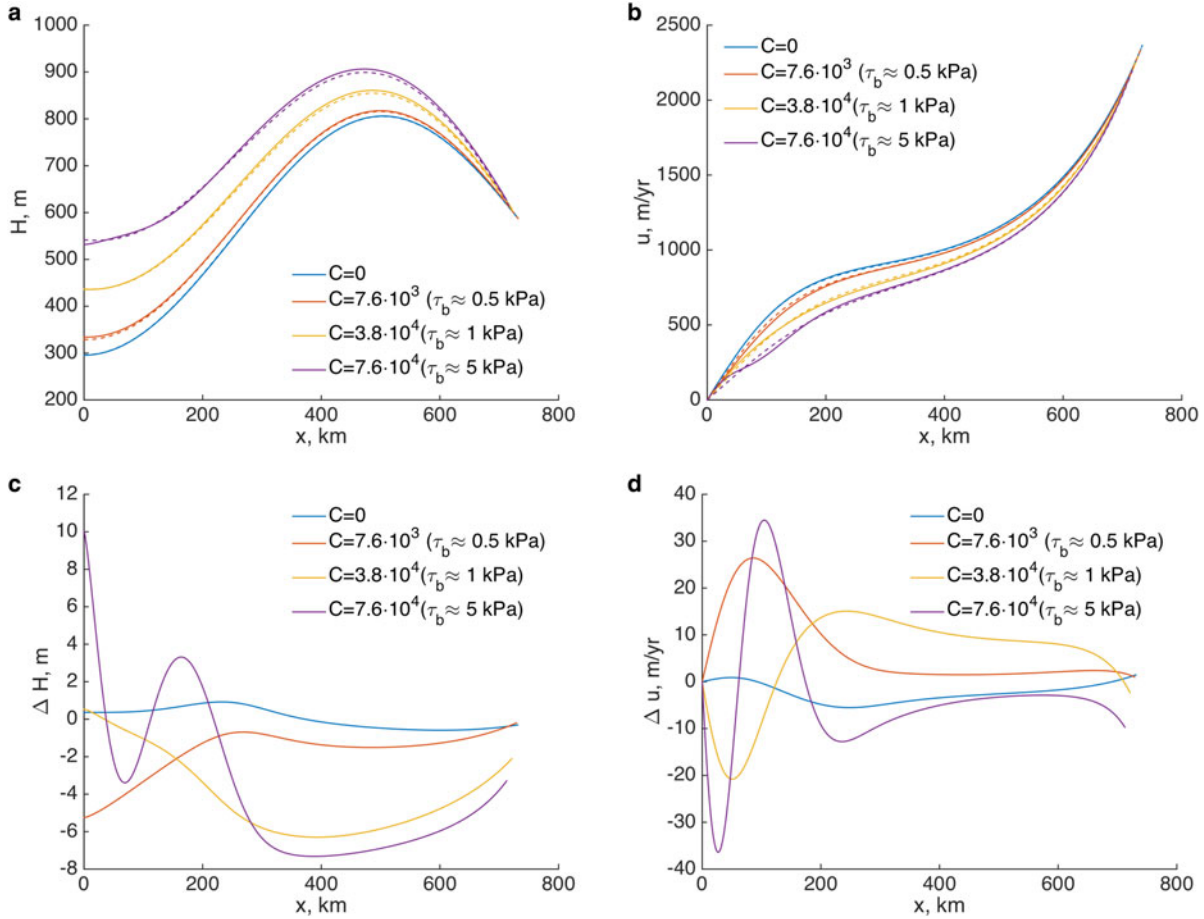


Fig. 8. Steady-state profiles of (a) ice thickness (m) and (b) ice velocity (m a^{-1}) computed for the same bed elevation and ice stiffness parameter as in Figure 3 and accumulation rate $\dot{a} = 1.9 \text{ m a}^{-1}$ analytically (solid lines) and numerically (dashed lines) for various values of the sliding coefficient C ($\text{Pa m}^{-1/3} \text{ s}^{1/3}$). (c) and (d) differences between numerical and analytical results: (c) ice thickness $\Delta h = h_{\text{numerical}} - h_{\text{analytical}}$ (m); (D) ice velocity $\Delta u = u_{\text{numerical}} - u_{\text{analytical}}$ (m a^{-1}).

and the expression for $(H_0|U_{0X}|^{(1/n)-1}U_{0X})_X$ is

$$(H_0|U_{0X}|^{(1/n)-1}U_{0X})_X = \frac{H_0^{n-3}}{n} |\dot{a}H_0^{n-1} - H_0^{n-2}QH_{0X}|^{(1/n)-1} \times [(n-2)H_{0X}(\dot{a}H_0 - QH_{0X}) + H_0(H_0\dot{a}_X - QH_{0XX})]. \quad (\text{A10})$$

Substituting these expressions into (A5a) and rearranging terms yield

$$H_{1X} = \frac{H_0^{-(n+2)/n}}{n} |\dot{a}H_0 - QH_{0X}|^{(1/n)-1} \left[(n-2)H_{0X}(\dot{a}H_0 - QH_{0X}) + H_0(H_0\dot{a}_X - QH_{0XX}) \right] - \Gamma \frac{Q^m}{H_0^{m+1}}. \quad (\text{A11})$$

To $O(\delta)$, the boundary condition (19d) is

$$H_0|U_{0X}|^{(1/n)-1}U_{0X} \left(1 + \frac{\delta U_{1X}}{n U_{0X}} \right) = \frac{H_0^2}{2} (1 + \delta). \quad (\text{A12})$$

Substituting (A9) and (A7) into (A12) and rearranging terms leads to

$$|\dot{a}H_0 - QH_{0X}|^{(1/n)-1} \left[\left(1 - \frac{\delta}{n} \right) (\dot{a}H_0 - QH_{0X}) - \frac{\delta}{n} Q(H_{1X} - H_{0X}) \right] = \frac{1 + \delta}{2} H_0^{(n+2)/n}, \quad X = X_g \quad (\text{A13})$$

where H_{1X} is defined by (A11) and H_0 is defined by (A2a). This equation implicitly defines the location of the grounding line X_g with Q expressed as $Q(X_g) = \int_0^{X_g} \dot{a} dx$.

The zeroth-order terms H_0 and U_0 are determined by (A2). The first-order term $H_1(X)$ is recovered by integrating expression (A11) with the boundary

condition (A5e) at $X = X_g$, and the first-order term $U_1(X)$ is determined by expression (A5b).

In order to assess the validity and accuracy of the approximate analytical expressions constructed above, we compare them with the 'exact', numerical solutions that are obtained using a finite-element solver COMSOL™ (COMSOL, 2018). In all simulations, the grid resolution is spatially variable: it is 200 m through 95% of the length of the domain, and 1 m in the 5% closest to the grounding line position x_g .

For a given bed elevation profile, $b(x)$, accumulation rate \dot{a} , (assumed to be constant), the sliding law parameters C and m (chosen to be $m = 1/n$), and ice stiffness parameter A , the grounding line position is determined from expression (29) (we use the Matlab™ routine `fzero` to find roots of (29)) and the h_k and u_k ($k = 0, 1$) are determined as described above. Unless otherwise noted, we use the bed elevation profile $b(x) = b_0 + b_a \cos(\pi x/L)$, with $b_0 = -500 \text{ m}$, $b_a = 250 \text{ m}$ and $L = 500 \text{ km}$, and the ice stiffness parameter $A = 1.35 \cdot 10^{-25} \text{ Pa}^{-3} \text{ s}^{-1}$ (which corresponds to $T_{\text{ice}} \approx -20^\circ \text{C}$).

Figure 8 shows numerical and analytical ice thickness and velocity profiles computed for various values of the sliding parameter C and the accumulation rate $\dot{a} = 1.89 \text{ m a}^{-1}$. The difference in the grounding line position computed with two methods is 738 m for $C=0$ and increases to 3.4 km for $C = 7.6 \cdot 10^4 \text{ Pa m}^{-1/3} \text{ s}^{1/3}$ (corresponds to a value of the non-dimensional parameter $\Gamma = 10$, Eqn (19a)) that are 0.16 and 0.47% respectively. The maximum difference in the ice thickness (Fig. 8c) and ice velocity (Fig. 8d) increases from 0.92 m and 2.76 m a^{-1} for $C=0$ to 10 m and 36.4 m a^{-1} for $C = 7.6 \cdot 10^4 \text{ Pa m}^{-1/3} \text{ s}^{1/3}$. This comparison suggests that the analytic expressions adequately approximate solutions of the problem (1), (5), (6)–(9) with sufficient accuracy.

Appendix B. Stability analysis

This section describes a stability analysis of steady-state solutions obtained in sections 'Steady states' and Appendix A 'Steady-state problem'. Small

deviations from a steady-state configuration can be written as

$$\begin{aligned} H &= H_{ss}(X) + \sigma \tilde{H}(X, T), \quad U = U_{ss}(X) + \sigma \tilde{U}(X, T), \\ X_g &= X_{gss} + \sigma \tilde{X}_g(T) \end{aligned} \quad (B1)$$

where H_{ss} , U_{ss} and X_{gss} are solutions of (19a), (21) and (19c)–(19e). Their substitution to the momentum and mass balances and boundary conditions (19) result in the following perturbation problem

$$\delta \left[\tilde{H} |U_{ssX}|^{(1/n)-1} U_{ssX} + \frac{1}{n} H_{ss} |U_{ssX}|^{(1/n)-1} \tilde{U}_X \right]_X - \tilde{H}_X H_{ss} - \tilde{H} (H_{ss} + B)_X - m \delta \Gamma |U_{ss}|^{m-1} \tilde{U} = 0 \quad (B2a)$$

$$\tilde{H}_T + (\tilde{U} H_{ss} + \tilde{H} U_{ss})_X = 0 \quad (B2b)$$

$$\tilde{H}_X = \tilde{U} = 0, \quad X = 0 \quad (B2c)$$

$$\begin{aligned} \frac{1}{n} H_{ss} |U_{ssX}|^{(1/n)-1} \tilde{U}_X + (H_{ss} |U_{ssX}|^{(1/n)-1} U_{ssX})_X \tilde{X}_g = \\ H_{ss} \left(H_{ssX} \tilde{X}_g + \frac{1}{2} \tilde{H} \right), \quad X = X_{gss} \end{aligned} \quad (B2d)$$

$$\tilde{H} + H_{ssX} \tilde{X}_g = -\frac{B_X}{1 - \delta} \tilde{X}_g, \quad X = X_{gss} \quad (B2e)$$

where (B2d) is obtained in the following way. To $O(\sigma)$

$$\begin{aligned} H |U_X|^{(1/n)-1} U_X \approx H_{ss} |U_{ssX}|^{(1/n)-1} U_{ssX} + \\ \sigma \left(\tilde{H} |U_{ssX}|^{(1/n)-1} U_{ssX} + \frac{1}{n} |U_{ssX}|^{(1/n)-1} \tilde{U}_X \right), \quad X = X_g \end{aligned} \quad (B3a)$$

$$\frac{H^2}{2} \approx \frac{1}{2} (H_{ss}^2 + 2\sigma \tilde{H} H_{ss}), \quad X = X_g \quad (B3b)$$

Because $H_{ss} |U_{ssX}|^{(1/n)-1} U_{ssX} = (H_{ss}^2/2)$, $\tilde{H} |U_{ssX}|^{(1/n)-1} U_{ssX} = \frac{1}{2} \tilde{H} H_{ss}$.

To $O(\sigma)$, $F(X_g) = F(X_{gss}) + \sigma \tilde{X}_g F_X(X_{gss})$, and the above expressions become

$$\begin{aligned} H |U_X|^{(1/n)-1} U_X \approx H_{ss} |U_{ssX}|^{(1/n)-1} U_{ssX} + \\ \sigma \left(\tilde{X}_g (H_{ss} |U_{ssX}|^{(1/n)-1} U_{ssX})_X + \tilde{H} |U_{ssX}|^{(1/n)-1} U_{ssX} + \frac{1}{n} H_{ss} |U_{ssX}|^{(1/n)-1} \tilde{U}_X \right), \\ X = X_{gss} \end{aligned} \quad (B4a)$$

$$\frac{H^2}{2} \approx \frac{1}{2} [H_{ss}^2 + 2\sigma (\tilde{X}_g H_{ss} H_{ssX} + \tilde{H} H_{ss})], \quad X = X_{gss} \quad (B4b)$$

Using the steady-state condition at X_{gss} , $H_{ss} |U_{ssX}|^{(1/n)-1} U_{ssX} = \frac{1}{2} H_{ss}^2$, the above expressions become (B2d).

As before, we write the steady-state solutions as

$$H_{ss} = H_{ss0} + \delta H_{ss1} + \dots \quad (B5a)$$

$$U_{ss} = U_{ss0} + \delta U_{ss1} + \dots \quad (B5b)$$

Substituting these expressions into the flotation condition (B2e) leads to

$$\tilde{X}_g \approx -\frac{1}{\delta} \frac{\tilde{H}}{B_X + H_{ss1X}}. \quad (B6)$$

Expression (B6) shows that \tilde{X}_g and \tilde{H} cannot be of the same order in δ . For \tilde{X}_g to be $O(1)$, \tilde{H} must be $O(\delta)$ to leading order and because of the mass balance (B2b) so does \tilde{U} . Hence, the series expansion of the perturbed variables should take a form

$$\tilde{H} = \delta \tilde{H}_1 + \delta^2 \tilde{H}_2 \dots \quad (B7a)$$

$$\tilde{U} = \delta \tilde{U}_1 + \delta^2 \tilde{U}_2 \dots \quad (B7b)$$

$$\tilde{X}_g = \tilde{X}_{g0} + \delta \tilde{X}_{g1} + \dots \quad (B7c)$$

Substitution of these and (B5) into the perturbation problem (B2) leads to the first-order problem

$$-\tilde{H}_{1X} H_{ss0} = 0 \quad (B8a)$$

$$\tilde{H}_{1T} + (\tilde{H}_1 U_{ss0} + \tilde{U}_1 H_{ss0})_X = 0 \quad (B8b)$$

$$\tilde{H}_{1X} = \tilde{U}_1 = 0, \quad X = 0 \quad (B8c)$$

$$\begin{aligned} \frac{1}{n} H_{ss0} |U_{ss0X}|^{(1/n)-1} \tilde{U}_{1X} + \tilde{X}_{g0} \left[H_{ss1} |U_{ss0X}|^{(1/n)-1} U_{ss0X} + \frac{1}{n} |U_{ss0X}|^{(1/n)-1} U_{ss1X} \right]_X = \\ \frac{1}{2} H_{ss0} \tilde{H}_1 + \tilde{X}_{g0} (H_{ss0} H_{ss1X} + H_{ss1} H_{ss0X}), \quad X = X_{gss} \end{aligned} \quad (B8d)$$

$$\tilde{X}_{g0} = -\frac{\tilde{H}_1}{H_{ss1X} + B_X} \quad (B8e)$$

The system (B8) is not as over-determined as it appears. Because $H_{ss0} \neq 0$, the momentum balance (B8a) reduces to $\tilde{H}_{1X} = 0$, and the first of the boundary conditions (B8c) is automatically satisfied. Solutions of (B8a) and (B8b) result in the following expressions for \tilde{H}_1 and \tilde{U}_1

$$\tilde{H}_1 = F(T) \quad (B9a)$$

$$\tilde{U}_1 = -\frac{1}{H_{ss0}} \left[\int_0^X dx \tilde{H}_{1T} + \tilde{H}_1 U_{ss0} \right] \quad (B9b)$$

where $F(T)$ is an arbitrary function of T determined from the boundary conditions and $\tilde{H}_{1T} = F'(T)$.

Expression for \tilde{U}_{1X} is determined from (B9b)

$$\tilde{U}_{1X} = \frac{H_{ss0X}}{H_{ss0}^2} \left[\int_0^X dx \tilde{H}_{1T} + \tilde{H}_1 U_{ss0} \right] - \frac{1}{H_{ss0}} [\tilde{H}_{1T} + \tilde{H}_1 U_{ss0X}] \quad (B10)$$

Using the zeroth-order steady-state condition (A1e),

$$\frac{1}{n} H_{ss0} |U_{ss0X}|^{(1/n)-1} = \frac{1}{2n} \frac{H_{ss0}^2}{U_{ss0X}} \quad (B11)$$

and substituting (B9a), (B10) and (B8c) to (B8d) leads to the following

equation for $F(T)$

$$\begin{aligned} \frac{H_{ss0}^2}{2nU_{ss0X}} \left[\frac{F'}{H_{ss0}^2} (H_{ss0X}X_{gss} - H_{ss0}) + \frac{F}{H_{ss0}^2} (H_{ss0X}U_{ss0} - H_{ss0}U_{ss0X}) \right] = \\ \frac{F}{H_{ss1X} + B_X} \left\{ \left[H_{ss1}|U_{ss0X}|^{(1/n)-1}U_{ss0X} + \frac{1}{n}|U_{ss0X}|^{(1/n)-1}U_{ss1X} \right]_X - \right. \\ \left. H_{ss0}H_{ss1X} + H_{ss1}H_{ss0X} \right\} + \frac{F}{2}H_{ss0} \end{aligned} \quad (B12)$$

After rearranging terms Eqn (B12) becomes

$$\begin{aligned} F' \left(H_{ss0X}X_{gss} - H_{ss0} \right) = -F \left\{ U_{ss0}H_{ss0X} - (n+1)H_{ss0}U_{ss0X} - \right. \\ \left. \frac{2nU_{ss0X}}{H_{ss1X} - H_{ss0X}} \left[\left(H_{ss1}|U_{ss0X}|^{(1/n)-1}U_{ss0X} + \frac{1}{n}H_{ss0}|U_{ss0X}|^{(1/n)-1}U_{ss1X} \right)_X - \right. \right. \\ \left. \left. H_{ss0} \left(H_{ss0X} + H_{ss1X} \right) \right] \right\}. \end{aligned} \quad (B13)$$

A solution of this equation is

$$F(T) = F(0)e^{\Lambda T} \quad (B14)$$

where

$$\begin{aligned} \Lambda = \left(H_{ss0} - H_{ss0X}X_{gss} \right)^{-1} \left\{ U_{ss0}H_{ss0X} - (n+1)H_{ss0}U_{ss0X} - \right. \\ \left. \frac{2nU_{ss0X}}{H_{ss1X} - H_{ss0X}} \left[\left(H_{ss1}|U_{ss0X}|^{(1/n)-1}U_{ss0X} + \frac{1}{n}H_{ss0}|U_{ss0X}|^{(1/n)-1}U_{ss1X} \right)_X - \right. \right. \\ \left. \left. H_{ss0} \left(H_{ss0X} + H_{ss1X} \right) \right] \right\} \end{aligned} \quad (B15)$$

The sign of the parameter Λ determines stability of the grounding line position: if perturbations from a steady-state configuration decay with time this configuration is stable, if they grow, it is unstable, i.e., for stable configurations $\Lambda < 0$ and for unstable configurations $\Lambda > 0$. Equation (B15) includes both the zeroth- and the first-order solutions of the steady-state problem. In order to express it through the parameters of the problem (e.g., bed elevation, accumulation rate, etc.) we substitute expressions for the steady-state terms obtained in Appendix A, and derive an expression for Λ using following intermediate steps. Using

$$\begin{aligned} \left(H_{ss1}|U_{ss0X}|^{(1/n)-1}U_{ss0X} + \frac{1}{n}H_{ss0}|U_{ss0X}|^{(1/n)-1}U_{ss1X} \right)_X = \\ H_{ss1X}|U_{ss0X}|^{(1/n)-1}U_{ss0X} + \frac{1}{n}|U_{ss0X}|^{(1/n)-1}U_{ss0XX} + \\ \frac{1}{n}H_{ss0X}|U_{ss0X}|^{(1/n)-1}U_{ss1X} + \frac{1}{n} \left(\frac{1}{n} - 1 \right) H_{ss0}|U_{ss0X}|^{(1/n)-2}U_{ss1X}U_{ss0XX} + \\ \frac{1}{n}H_{ss0}|U_{ss0X}|^{(1/n)-1}U_{ss1XX} \end{aligned} \quad (B16)$$

and rearranging terms

$$\begin{aligned} \Lambda = \left(H_{ss0} - H_{ss0X}X_{gss} \right)^{-1} \left\{ U_{ss0}H_{ss0X} - H_{ss0}U_{ss0X} + \frac{3nH_{ss0}H_{ss0X}U_{ss0X}}{H_{ss1X} - H_{ss0X}} - \right. \\ \left. \frac{H_{ss0}}{H_{ss1X} - H_{ss0X}} \left[H_{ss0}(U_{ss0XX} + U_{ss1XX}) + H_{ss0X}U_{ss1X} + \right. \right. \\ \left. \left. 2 \left(\frac{1}{n} - 1 \right) |U_{ss0X}|^{(1/n)-1}U_{ss0XX}U_{ss1X} \right] \right\}. \end{aligned} \quad (B17)$$

With

$$\begin{aligned} U_{ss1XX} = -U_{ss0XX} \frac{H_{ss1}}{H_{ss0}} - 2 \frac{U_{ss0X}}{H_{ss0}} \left(H_{ss1X} - H_{ss0X} \frac{H_{ss1}}{H_{ss0}} \right) + \\ 2 \frac{U_{ss0}H_{ss0X}}{H_{ss0}^2} \left(H_{ss1X} - H_{ss0X} \frac{H_{ss1}}{H_{ss0}} \right) - \frac{U_{ss0}}{H_{ss0}} \left(H_{ss1XX} - H_{ss0XX} \frac{H_{ss1}}{H_{ss0}} \right) \end{aligned} \quad (B18a)$$

$$\begin{aligned} U_{ss1XX}(X_{gss}) = -U_{ss0XX} - 2 \frac{U_{ss0X}}{H_{ss0}} (H_{ss1X} - H_{ss0X}) + \\ 2 \frac{U_{ss0}H_{ss0X}}{H_{ss0}^2} (H_{ss1X} - H_{ss0X}) - \frac{U_{ss0}}{H_{ss0}} (H_{ss1XX} - H_{ss0XX}) \end{aligned} \quad (B18b)$$

the above expression becomes

$$\begin{aligned} \Lambda = \left(H_{ss0} - H_{ss0X}X_{gss} \right)^{-1} \left\{ H_{ss0}U_{ss0X} - U_{ss0}H_{ss0X} + \frac{3nH_{ss0}H_{ss0X}U_{ss0X}}{H_{ss1X} - H_{ss0X}} - \right. \\ \left. \frac{H_{ss0}}{H_{ss1X} - H_{ss0X}} \left[U_{ss0}(H_{ss0XX} - H_{ss1XX}) + H_{ss0X}U_{ss1X} + \right. \right. \\ \left. \left. 2 \left(\frac{1}{n} - 1 \right) |U_{ss0X}|^{(1/n)-1}U_{ss0XX}U_{ss1X} \right] \right\}. \end{aligned} \quad (B19)$$

Using Eqn (A7) for $U_{ss1X}(X_{gss})$ and the steady-state boundary condition (A1e) again

$$\begin{aligned} \Lambda = \left(H_{ss0} - H_{ss0X}X_{gss} \right)^{-1} \left\{ H_{ss0}U_{ss0X} + \frac{(3n+1)H_{ss0}H_{ss0X}U_{ss0X}}{H_{ss1X} - H_{ss0X}} + \right. \\ \left(\frac{1}{n} - 1 \right) U_{ss0}H_{ss0} \frac{U_{ss0XX}}{U_{ss0X}} - \frac{H_{ss0}}{H_{ss1X} - H_{ss0X}} \times \\ \left[U_{ss0} \left(H_{ss0XX} - H_{ss1XX} \right) - \left(\frac{1}{n} - 1 \right) H_{ss0}U_{ss0XX} \right] \right\}. \end{aligned} \quad (B20)$$

With

$$\begin{aligned} U_{ss0XX} = \left(\frac{\dot{a}}{H_{ss0}} - U_{ss0} \frac{H_{ss0X}}{H_{ss0}} \right)_X = \\ \frac{1}{H_{ss0}} (\dot{a}_X - 2U_{ss0X}H_{ss0X} - U_{ss0}H_{ss0XX}) \end{aligned} \quad (B21)$$

Λ can be expressed as

$$\begin{aligned} \Lambda = \left(H_{ss0} - H_{ss0X}X_{gss} \right)^{-1} \left\{ H_{ss0}U_{ss0X} - 2 \left(\frac{1}{n} - 1 \right) U_{ss0}H_{ss0X} + \right. \\ \frac{(3n - \frac{2}{n} + 3)H_{ss0}H_{ss0X}U_{ss0X}}{H_{ss1X} - H_{ss0X}} + \left(\frac{1}{n} - 1 \right) \frac{U_{ss0}}{U_{ss0X}} (\dot{a}_X - U_{ss0}H_{ss0XX}) - \\ \left. \frac{H_{ss0}}{H_{ss1X} - H_{ss0X}} \left[U_{ss0} \left(\frac{1}{n}H_{ss0XX} - H_{ss1XX} \right) - \left(\frac{1}{n} - 1 \right) \dot{a}_X \right] \right\}. \end{aligned} \quad (B22)$$

Using expression (A8) for $U_{ss0X}(X_g)$ and rearranging terms

$$\begin{aligned} \Lambda = \left(H_{ss0} - H_{ss0X}X_{gss} \right)^{-1} \left\{ \dot{a} - \left(\frac{2}{n} - 1 \right) U_{ss0}H_{ss0X} + \right. \\ \left(3n - \frac{2}{n} + 3 \right) \frac{H_{ss0X}(\dot{a} - U_{ss0}H_{ss0X})}{H_{ss1X} - H_{ss0X}} + \\ \left(\frac{1}{n} - 1 \right) H_{ss0}U_{ss0} \frac{\dot{a}_X - U_{ss0}H_{ss0XX}}{\dot{a} - U_{ss0}H_{ss0X}} - \frac{H_{ss0}}{H_{ss1X} - H_{ss0X}} \times \\ \left[U_{ss0} \left(\frac{1}{n}H_{ss0XX} - H_{ss1XX} \right) - \left(\frac{1}{n} - 1 \right) \dot{a}_X \right] \right\} \end{aligned} \quad (B23)$$

where

$$\begin{aligned}
 H_{ss1XX} = & \frac{H_{ss0}^{-\frac{n+2}{n}}}{n} \left| \dot{a}H_{ss0} - Q_{gss}H_{ss0X} \right|^{\frac{1}{n}-1} \left[(n-2) \left(\dot{a}H_{ss0} - Q_{gss}H_{ss0X} \right) \times \right. \\
 & \left(H_{ss0XX} - \frac{n+2H_{ss0X}}{n} \frac{H_{ss0}}{H_{ss0}} \right) + (H_{ss0}\dot{a}_X - Q_{gss}H_{ss0XX}) \left\{ \left(1+n-\frac{2}{n} \right) H_{ss0X} + \right. \\
 & \left. \left(\frac{1}{n}-1 \right) H_{ss0} \frac{H_{ss0}\dot{a}_X - Q_{gss}H_{ss0XX}}{\dot{a}H_{ss0} - Q_{gss}H_{ss0X}} - \frac{n+2}{n} \right\} + \\
 & \left. H_{ss0} \left(\dot{a}_X H_{ss0X} + \dot{a}_{XX} H_{ss0} - \dot{a}H_{ss0XX} - Q_{gss}H_{ss0XXX} \right) \right] - \\
 & m\Gamma \left| U_{ss0} \right|^{m-1} \frac{U_{ss0X}}{H_{ss0}} + \Gamma \left| U_{ss0} \right|^{m-1} U_{ss0} \frac{H_{ss0X}}{H_{ss0}^2}.
 \end{aligned}$$

(B24)

In terms of $Q_{gss} = \int_0^{X_{gss}} \dot{a} dx$ this expression is

$$\begin{aligned}
 \Lambda = & \left(H_{ss0} - H_{ss0X} X_{gss} \right)^{-1} \left\{ \dot{a} - \left(\frac{2}{n} - 1 \right) \frac{Q_{gss}}{H_{ss0}} H_{ss0X} + \right. \\
 & \left(3n - \frac{2}{n} + 3 \right) \frac{H_{ss0X} \left(H_{ss0}\dot{a} - Q_{gss}H_{ss0X} \right)}{H_{ss0} \left(H_{ss1X} - H_{ss0X} \right)} + \\
 & \left(\frac{1}{n} - 1 \right) Q_{gss} \frac{H_{ss0}\dot{a}_X - Q_{gss}H_{ss0XX}}{H_{ss0}\dot{a} - Q_{gss}H_{ss0X}} - \\
 & \left. \frac{1}{H_{ss1X} - H_{ss0X}} \left[Q_{gss} \left(\frac{1}{n} H_{ss0XX} - H_{ss1XX} \right) - \left(\frac{1}{n} - 1 \right) H_{ss0}\dot{a}_X \right] \right\}
 \end{aligned}$$

(B25)

The dimensional form of Λ is expression (36).